ON THE STRUCTURE OF ACCRETION DISKS WITH OUTFLOWS

Cheng-Liang Jiao[1] and Xue-Bing Wu[2]
Department of Astronomy, School of Physics, Peking University, Beijing 100871, China

ABSTRACT

In order to study the outflows from accretion disks, we solve the set of hydrodynamic equations for accretion disks in the spherical coordinates ($r\theta\phi$) to obtain the explicit structure along the θ direction. Using self-similar assumptions in the radial direction, we change the equations to a set of ordinary differential equations (ODEs) about the θ-coordinate, which are then solved with symmetrical boundary conditions in the equatorial plane, and the velocity field is obtained. The α viscosity prescription is applied and an advective factor f is used to simplify the energy equation.The results display thinner, quasi-Keplerian disks for Shakura-Sunyaev Disks (SSDs) and thicker, sub-Keplerian disks for Advection Dominated Accretion Flows (ADAFs) and slim disks, which are consistent with previous popular analytical models. However, an inflow region and an outflow region always exist, except when the viscosity parameter α is too large, which supports the results of some recent numerical simulation works. Our results indicate that the outflows should be common in various accretion disks and may be stronger in slim disks, where both advection and radiation pressure are dominant. We also present the structure dependence on the input parameters and discuss their physical meanings. The caveats of this work and possible improvements in the future are discussed.

Subject headings: accretion, accretion disks - hydrodynamics - black hole physics

1. INTRODUCTION

The accretion disk models have been developed much in the past several decades. Many disk models have been proposed and some of them are widely adopted in astrophysical studies nowadays, including but not restricted to Shakura-Sunyaev Disk (SSD; see Shakura & Sunyaev 1973),

[1]E-mail: chengliang.jiao@pku.edu.cn

[2]E-mail: wuxb@pku.edu.cn

Advection Dominated Accretion Flow (ADAF; see Narayan & Yi 1994; Abramowicz et al. 1995), and slim disk (Abramowicz et al. 1988). However, the outflow structure of accretion disks still remains an open problem. The equations that describe the hydrodynamic processes are the Navier-Stokes equations, which are quite difficult to solve in the case of accretion disks which involve viscosity and radiation. Therefore, in most works, some kind of simplification, such as one-zone or polytropic distribution and hydrostatic equilibrium, are usually applied in the vertical direction, and the vertical variation (z dependence in cylindrical coordinates) of the velocity field is usually neglected. In this way the equations are changed to a set of ordinary differential equations (ODEs) in the radial direction, which can be solved numerically. However, by taking these assumptions, one cannot get a clear picture of the vertical structure of accretion flows; the velocity is always radially inward and no mass will cross the disk surface, displaying no outflow structure. Among the exceptions is a work done by Narayan & Yi in 1995(hereafter NY95), which used self-similar assumptions in the radial direction and solved the structure along the θ direction in spherical coordinates ($r\theta\phi$). However, in their work they assumed $v_\theta = 0$ and thus cannot get a proper velocity field, and their solutions compose of only pure inflow. They argued that the Bernoulli parameter is positive in their solutions so that a bipolar outflow is expected to develop near the vertical axis. Blandford & Begelman (1999, hereafter BB99) relaxed the mass conservation assumption and assumed that the mass inflow rate varies with radius, and obtained solutions with outflow called adiabatic inflow-outflow solutions (ADIOS). Their solutions are one-dimensional self-similar solutions that are height-averaged and they also applied the Bernoulli parameter to argue the presence of outflow. However, Abramowicz et al.(2000) pointed out that the positive Bernoulli function (instead of Bernoulli parameter, which is defined in convenience of self-similar assumptions) is not sufficient for outflow (also see the simulation works done by Stone et al. 1999 and Yuan & Bu 2010). Blandford & Begelman (2004) furthered their work and presented some self-similar two-dimensional solutions of radiatively inefficient accretion flows with outflow. They assumed hydrostatic equilibrium in the vertical direction and that convection dominates the heat transport, which may only be applicable in certain cases. Xu & Chen (1997, hereafter XC97) relaxed $v_\theta = 0$ and obtained two types of solutions with outflow: accretion and ejection solutions. However their solutions require the net accretion rate to be 0, which is not realistic. Xue & Wang(2005, hereafter XW05) followed NY95 and solved the disk structure along the θ direction considering v_θ. They arbitrarily set a disk surface, at which $v_r = 0$, and the sound speed on the surface for their calculation. Their solutions display a field of inflow near the equatorial plane with wind blowing out of the upper boundary, however the boundary is set as an input parameter rather than being calculated, and they only investigated several cases of ADAFs. In §3.2 we will see that according to our calculation, their assumption doesn't hold for accretion flows with large α value. Sadowski et al.(2010) abandoned the self-similar assumptions and solved the accretion disk structure in the radial and vertical direction simultaneously. Because the Navier-Stokes equations for accretion disks cannot be decoupled intrinsically, they adopted other assumptions, e.g. the disk is not geometrically thick,

to derive the equations. As in their work they didn't consider v_z while v_r and v_ϕ were supposed not to vary vertically, they were not able to study outflows. In summary, in the analytical model study, the vertical or θ-direction structure of accretion disks and outflows can still not be dealt with satisfactorily, and many improvements are still needed to be made.

On the other hand, observationally there are more and more evidences for outflows in accretion systems, such as Sgr A*(Marrone et al. 2006; Xie & Yuan 2008), soft X-ray transients(Loeb et al. 2001) and quasars with blueshifted absorption lines(e.g., PG1115+80; Chartas et al. 2003). Many numerical simulation works have also discovered outflows in their results (e.g. Stone et al., 1999; Igumenshchev & Abramowicz, 2000; Okuda et al. 2005; Ohsuga et al.2005; Ohsuga & Mineshige 2007; Ohsuga et al. 2009) . The common existence of outflows in these works inspire us to investigate the vertical structure of accretion flows explicitly, to find solutions which can deal with v_θ and positive v_r to get a clear velocity field, and with more reasonable boundary conditions. As a first step, we followed the work done by NY95 and XW05, using self-similar assumptions in the radial direction and solving the ODEs along the θ direction in spherical coordinates ($r\theta\phi$). We used the α viscosity prescription and assumed that the $r\phi$ component of the viscosity stress tensor is dominant. By neglecting other components of the viscosity stress tensor, the necessary number of boundary conditions is reduced and we will only need the boundary conditions in the equatorial plane, which is obatined by symmetry and is thus quite physical. As we didn't set other arbitrary restrictions to v_r and v_θ other than the self-similar assumptions, we can get a velocity field containing positive v_r, to discuss the flow structure with possible outflows. These assumptions are applicable to different kinds of accretion disk models, ranging through SSD, ADAF and slim disk, so we also did many calculations with different sets of parameters (which is very difficult to do in a numerical simulation work as it would be too time-consuming), trying to find the flow structure dependence on the parameters, in order to understand the inflow/outflow mechanism more physically. These results can also be helpful to future numerical simulation works when they set the input parameters.

It should be noted that there is another branch of researches which investigate accretion flows with an outflow (usually wind) plus accretion disk model. In these researches, the configuration of the outflow and accretion disk is usually preset, and the calculations are focused on either the outflow or the accretion disk while the influence of the other part is simplified or parameterized (e.g. Fukue, 1989; Takahara et al., 1989; Kusunose, 1991; BB99; Misra & Taam, 2001; Fukue, 2004; Xie & Yuan, 2008). Recently there are also several works done in this way which deal with the outflow and the accretion disk simultaneously (Kawabata & Mineshige, 2009; Dotan & Shaviv, 2010). Compared with our work, in these studies the accretion disk is usually height-integrated and the configuration of the accretion flow is assumed rather than being calculated, while in our work we solve the full hydrodynamic equations to get the configuration of the accretion flow. Our work focuses on studying the general structure of disks, outflows and the physical mechanism behind

them, and the results can be complementary to one another.

In §2 we present the basic equations and assumptions we used in our calculations. In §3.1 we discuss our numerical methods and present solutions corresponding to typical parameters of SSD, ADAF and slim disk. In §3.2 we show the disk structure dependence on different parameters and discuss their physical meanings. In §4 we present our summary and discussion.

2. EQUATIONS AND ASSUMPTIONS

We consider the hydrodynamic equations of an accretion flow in the spherical coordinates $(r\theta\phi)$. The flow is assumed to be steady($\partial/\partial t = 0$) and axisymmetric($\partial/\partial\phi = 0$). Thus the continuity equation can be written as

$$\frac{1}{r^2}\frac{\partial}{\partial r}(r^2\rho v_r) + \frac{1}{r\sin\theta}\frac{\partial}{\partial\theta}(\sin\theta\rho v_\theta) = 0. \tag{1}$$

We assume that for the accretion flow, only the $r\phi$-component of the viscous tensor, $t_{r\phi}$, is dominant. And we use the Newtonian gravitational potential, $\Phi = -GM/r$. Then the equations of motion can be written as(Kato et al. 2008, also see Appendix A of XW05)

$$v_r\frac{\partial v_r}{\partial r} + \frac{v_\theta}{r}(\frac{\partial v_r}{\partial\theta} - v_\theta) - \frac{v_\phi^2}{r} = -\frac{GM}{r^2} - \frac{1}{\rho}\frac{\partial p}{\partial r} \tag{2}$$

$$v_r\frac{\partial v_\theta}{\partial r} + \frac{v_\theta}{r}(\frac{\partial v_\theta}{\partial\theta} + v_r) - \frac{v_\phi^2}{r}\cot\theta = -\frac{1}{\rho r}\frac{\partial p}{\partial\theta} \tag{3}$$

$$v_r\frac{\partial v_\phi}{\partial r} + \frac{v_\theta}{r}\frac{\partial v_\phi}{\partial\theta} + \frac{v_\phi}{r}(v_r + v_\theta\cot\theta) = \frac{1}{\rho r^3}\frac{\partial}{\partial r}(r^3 t_{r\phi}) \tag{4}$$

In our calculation, we adopt the α prescription of viscosity $t_{r\phi} = -\alpha p$ and p is the total pressure. The shearing box radiation Magnetohydrodynamics (MHD) simulations done by Hirose et al. (2009) found that the vertically integrated stress is approximately proportional to the vertically averaged total thermal (gas plus radiation) pressure. In our work, however, we also apply this relation locally.

Following NY95, we use the advective factor, $f \equiv Q_{\rm adv}/Q_{\rm vis}$, i.e. a fraction f of the dissipated energy is advected as stored entropy and a fraction $(1-f)$ is lost due to radiation. In our calculation we assume that f is constant in the accretion flow, so the energy equation can be written as

$$\rho(v_r\frac{\partial e}{\partial r} + \frac{v_\theta}{r}\frac{\partial e}{\partial\theta}) - \frac{p}{\rho}(v_r\frac{\partial\rho}{\partial r} + \frac{v_\theta}{r}\frac{\partial\rho}{\partial\theta}) = f t_{r\phi} r\frac{\partial}{\partial r}(\frac{v_\phi}{r}), \tag{5}$$

where e is the internal energy of the material and can be expressed as(Kato et al. 2008)

$$\rho e = \frac{p_{\rm gas}}{\gamma - 1} + 3p_{\rm rad}, \tag{6}$$

where γ is the heat capacity ratio and is considered to be a constant input parameter in our calculation.

We adopt the self-similar assumptions in the radial direction, therefore we seek a solution of the form

$$\rho = \rho(\theta) r^{-n}, \tag{7}$$

$$v_r = v_r(\theta)\sqrt{\frac{GM}{r}}, \tag{8}$$

$$v_\theta = v_\theta(\theta)\sqrt{\frac{GM}{r}}, \tag{9}$$

$$v_\phi = v_\phi(\theta)\sqrt{\frac{GM}{r}}, \tag{10}$$

$$p = p(\theta) GM r^{-n-1}. \tag{11}$$

This set of self-similar solutions is similar to that of NY95 and is actually identical to that of XW05. Compared with those works, here we use the total pressure p in Equation (11) instead of the sound speed c_s, which is proportional to $\sqrt{p/\rho}$. As stated in NY95, the only length scale in the problem is r and the only frequency is $\Omega_{\rm K}$, thus all velocities must scale with radius as $r\Omega_{\rm K}$. In NY95, Narayan and Yi set $n = 3/2$, which implies $v_\theta = 0$ according to the continuity equation, thus they intrinsically set no outflow for the accretion disk. Here we relax this parameter n following BB99 and XW05, to allow outflows from the disk.

If we substitute Equations (7)-(11) into Equations (1)-(4), the r components can be eliminated, leaving only the dimensionless fuctions $\rho(\theta)$, $v_r(\theta)$, $v_\theta(\theta)$, $v_\phi(\theta)$, $p(\theta)$, the variable θ and some constants which are set as input parameters. The energy equation (Equation (5)) is somewhat more complex. As the internal energy depends differently on gas pressure and radiation pressure, we discuss the energy equation more carefully here. First, one may notice that only the total pressure p appears in Equations (1)-(4). This is not hard to understand as the dynamical processes don't recognize whether the pressure is from gas or radiation. $p_{\rm gas}$ and $p_{\rm rad}$ do affect the energy equation in a different way, and to describe this effect, we define the gas pressure ratio β,

$$\beta \equiv \frac{p_{\rm gas}}{p} = \frac{p_{\rm gas}}{p_{\rm gas} + p_{\rm rad}}. \tag{12}$$

There is one particular case that when $\gamma = 4/3$, no matter what the value of β is, the solution remains the same, as in this case Equation (6) becomes $\rho e = 3p$; if the accretion flow is radiation

pressure dominated ($\beta \to 0$), then Equation (6) also becomes $\rho e = 3p$, and the flow structure won't depend on γ; if the accretion flow is gas pressure dominated, then Equation (6) becomes $\rho e = p/(\gamma - 1)$, and the result will depend on the value of γ. For a general case, Equation (6) can be written as

$$\rho e = \frac{p_{\rm gas}}{\gamma - 1} + 3p_{\rm rad} = \left[\frac{\beta}{\gamma - 1} + 3(1 - \beta)\right] p. \tag{13}$$

Physically β is a value between 0 and 1, so ρe is always between $3p$ and $p/(\gamma - 1)$. Then we can expect that a general solution should be somewhere between two extreme cases: the gas pressure dominated case and the radiation pressure dominated case. For these two extreme cases, we can calculate the exact solutions of the problem, as Equation (6) will be simplified to forms without β. These two cases also provide the typical solutions we emphasize in §3.1. However we also want to know how the solutions change from the gas pressure dominated case to the radiation pressure dominated case. For the accretion flows in which both gas pressure and radiation pressure are important, we have to assume the gas pressure ratio β to be constant to solve the problem. Solving the problem with variant β is beyond the capability of this self-similar treatment, and we're planning to do that in our next work.

As we already mentioned, the radiation pressure dominated case has the same result as that of the gas pressure dominated case with $\gamma = 4/3$, so the question eventually becomes examining how the solution changes according to γ for the gas pressure dominated case. We define an equivalent γ here

$$\gamma_{\rm equ} \equiv \frac{p}{\rho e} + 1 = \frac{\gamma - 1}{\beta + 3(1 - \beta)(\gamma - 1)} + 1, \tag{14}$$

so that Equation (6) becomes

$$\rho e = \frac{p}{\gamma_{\rm equ} - 1}, \tag{15}$$

and this $\gamma_{\rm equ}$ represents the equivalent γ that the accretion flow would have if the flow is treated as gas pressure dominated (even $\beta \neq 1$). We can see that if the flow is radiation pressure dominated ($\beta = 0$), then no matter what the value of γ is, $\gamma_{\rm equ}$ is always 4/3. Here we treat γ as a constant, and for any specific case, we can get a constant $\gamma_{\rm equ}$ and all the situations can be treated as a gas pressure dominated flow with $\gamma_{\rm equ}$ as an input parameter. Usually γ is taken as a value between 7/5(the value for diatomic ideal gas) and 5/3(the value for monatomic ideal gas), so that $\gamma_{\rm equ}$ ranges between 4/3 and 5/3.

With Equations (7)-(11) and (15), the Equations (1)-(5) can be reduced to a set of five ODEs:

$$2v_\theta(\theta)\frac{d\rho(\theta)}{d\theta} + \rho(\theta)\left[(3 - 2n)v_r(\theta) + 2\left(\cot\theta v_\theta(\theta) + \frac{dv_\theta(\theta)}{d\theta}\right)\right] = 0, \tag{16}$$

$$2(n+1)p(\theta)+\rho(\theta)\left[v_r(\theta)^2+2\left(-1+v_\theta(\theta)^2+v_\phi(\theta)^2-v_\theta(\theta)\frac{dv_r(\theta)}{d\theta}\right)\right]=0, \tag{17}$$

$$2\frac{dp(\theta)}{d\theta}+\rho(\theta)\left[-2\cot\theta v_\phi(\theta)^2+v_\theta(\theta)\left(v_r(\theta)+2\frac{dv_\theta(\theta)}{d\theta}\right)\right]=0, \tag{18}$$

$$-2(n-2)\alpha p(\theta)+\rho(\theta)\left[v_r(\theta)v_\phi(\theta)+2v_\theta(\theta)\left(\cot\theta v_\phi(\theta)+\frac{dv_\phi(\theta)}{d\theta}\right)\right]=0, \tag{19}$$

$$2\rho(\theta)v_\theta(\theta)\frac{dp(\theta)}{d\theta}+p(\theta)\left\{\rho(\theta)\left[2(n\gamma_{\rm equ}-n-1)v_r(\theta)-3\alpha f(\gamma_{\rm equ}-1)v_\phi(\theta)\right]-2\gamma_{\rm equ}v_\theta(\theta)\frac{d\rho(\theta)}{d\theta}\right\}=0, \tag{20}$$

with 5 dimensionless fuctions $\rho(\theta)$, $v_r(\theta)$, $v_\theta(\theta)$, $v_\phi(\theta)$, $p(\theta)$, the variable θ and four input parameters ($\alpha, f, \gamma_{\rm equ}, n$). This set of ODEs can be numerically solved with proper boundary conditions. We assume the structure of the disk is symmetric to the equatorial plane, and thus we have

$$\theta=90^{\rm o}: v_\theta=\frac{d\rho}{d\theta}=\frac{dp}{d\theta}=\frac{dv_r}{d\theta}=\frac{dv_\phi}{d\theta}=0 \tag{21}$$

in which only four conditions are independent. For the last boundary condition we set $\rho(90^{\rm o})=1$, which can be normalized by a scale factor if the effective accretion rate at a certain radius is set (NY95, XW05, etc.). These boundary conditions are enough for our calculations and we didn't introduce other arbitrary boundary conditions.

3. NUMERICAL RESULTS

3.1. Typical Solutions

We obtained numerical solutions of Equations (16)-(20) with different sets of input parameters ($\alpha, f, \gamma_{\rm equ}, n$). Some typical solutions are shown in Figures 1-4. The calculation starts from the equatorial plane ($\theta = 90^{\rm o}$) towards the vertical axis ($\theta = 0^{\rm o}$). Generally the mass density ρ and total pressure p will decrease as θ decreases, and at certain inclination they will get very close to 0 as shown in the figures. We take this as the upper boundary of the flow structure. If we continue the calculation through this inclination, it will encounter numerical errors. We think the reason is that we can't describe the flow near the vertical axis with a simple self-similar solution in the radial direction. This effect is also to be expected. If we describe the upper boundary (minimum θ) that

we reach in our calculation as $\theta_{\rm b}$, then the effective accretion rate $\dot{M}_{\rm eff}$ across a sphere at radius r within the region calculated by us is

$$\dot{M}_{\rm eff} = 2\int_{\theta_{\rm b}}^{90^{\rm o}} \rho v_r \cdot 2\pi r \sin\theta r \cdot (\pi/180^{\rm o}) d\theta = 4\pi\sqrt{GM} r^{\frac{3}{2}-n} \int_{\theta_{\rm b}}^{90^{\rm o}} v_r(\theta)\rho(\theta)\sin\theta \cdot (\pi/180^{\rm o}) d\theta, \quad (22)$$

which is a function of r unless $n = 3/2$. In Equation (22) (and subsequently in this paper) negative values of $\dot{M}_{\rm eff}$ represent inflow while positive values represent outflow. If we describe the accretion rate in the region between the vertical axis and the inclination $\theta_{\rm b}$ as $\dot{M}_{\rm axis}$, then according to the steady nature of the flow, we have

$$\dot{M}_{\rm eff} + \dot{M}_{\rm axis} = \dot{M} \quad (23)$$

in which $\dot{M}$ represents the total accretion rate across any sphere at a reasonable radius centered by the central accretor and should be a constant for a steady accretion flow. If the solution doesn't end at an upper boundary, and instead can describe the entire flow structure in the whole space, then $\theta_{\rm b} = 0$ and $\dot{M}_{\rm eff} = \dot{M}$, which should be a constant. According to Equation (22), this can only happen in the following two cases: (1) $n = 3/2$ which enforces $\dot{M}_{\rm eff}$ not to change with radius r; (2) when $n \neq 3/2$, the integration term in Equation (22) must be 0, in which case $\dot{M}_{\rm eff} = 0$ and is a constant along radius r. The first case was discussed in NY95. Because $n = 3/2$, $r^2\rho v_r$ is independent of r, and the continuity equation (1) shows that $v_\theta = 0$, resulting in a solution in which the flow is always radial (with rotation). The second case was discussed in XC97, and the fact that $\dot{M} = 0$ requires that the outflow rate exactly equals the inflow rate at any radius. However this is unrealistic for an accretion flow, which is also discussed in XW05. The reason is that, when material is accreted in the form of an accretion flow, gravitational energy is released and part of it is changed to internal energy via viscous friction. The restriction that outflow rate equals inflow rate requires that the internal energy released from gravitational energy should be fully returned to gravitational energy, which violates the second law of thermodynamics. Therefore, the inflow rate must be larger than the outflow rate at a certain radius, in order to compensate for the increase in entropy in the hydrodynamic process. As we have mentioned before, there are many observations of accretion systems with outflows, and they can be neither of the two cases mentioned above (case (1) has no outflow while case (2) violates the second law of thermodynamics). So the self-similar solutions for an accretion disk with outflow have to be truncated at some inclination. It should be noted that this effect has already been discussed in XW05, though they assumed that the self-similar solution is only valid for the inflow part. Our solutions, however, show that at least part of the outflow (with $\theta_{\rm b} < \theta < \theta_0$) can be described with self-similar assumptions.

From the above analysis, we can also see that n is a very important parameter. When $n = 3/2$, the entire flow structure can be described by the same set of self-similar solutions, however this kind of solutions have no outflow. When $n \neq 3/2$, self-similar solutions can only describe part of the entire flow structure. According to Equation (22), when $n < 3/2$, the effective accretion rate

$\dot{M}_{\rm eff}$ decreases as r decreases, implying that material is lost due to outflows. This kind of solutions contain outflows, which is also consistent with the results of many numerical simulation works (e.g. Okuda et al. 2005; Ohsuga et al.2005; Ohsuga & Mineshige 2007; Ohsuga et al. 2009). On the other hand, when $n > 3/2$, the solutions have an effective accretion rate $\dot{M}_{\rm eff}$ that increases towards the central accretor, which implies that there must be matter injection into the accretion flow from high latitudes. This kind of matter injection is not likely to happen in real cases. So we would like to investigate solutions with $n \leqslant 3/2$. Solutions with $n = 3/2$ have been examined in NY95, and they are only for ADAFs, while solutions with $n < 3/2$ in our work is applicable to a much wider range of accretion disk types. So in this subsection, we take $n = 1.3$ to calculate the typical solutions. In this way we can observe how the solutions differ from those of $n = 3/2$ when n doesn't change much. We also calculated how the solutions change with different n, which will be discussed in detail in §3.2. The result shows that, when other parameters are the same, for a large range of n with $n < 3/2$ the solutions display similar structures qualitatively.

The value of the viscosity parameter α can be inferred both from observations and from MHD simulations of magneto-rotational instability (MRI). As reviewed by King et al. (2007), the value of α for ionized disks given by numerical simulations is ~ 0.01, while that obtained through observations is $\sim 0.1 - 0.4$. However, the observational determinations of α are strongly model-dependent and it still remains an open question what the value of α should be for hot, ionized disks. In this subsection we take $\alpha = 0.1$, which is a typical value used in theoretical models of accretion disks. We also discussed how the solutions would change with different α in §3.2.

Among the most popular analytical disk models are the SSD, ADAF and slim disk models, so here we show the solutions with input parameter corresponding to them respectively. For accretion flows composed mostly of fully ionized hydrogen, the material can be regarded as monatomic ideal gas, of which $\gamma = 5/3$, and that is the value we take here (accretion flows composed of unionized H_2 would have $\gamma = 7/5$. We didn't discuss this situation here, but some relative results can be found in §3.2). Figures 1 & 2 are both for the SSD model which has little advection ($f = 0.01$), while Figure 1 is for the gas pressure dominated region and Figure 2 for the radiation pressure dominated region. The ADAF model is treated as advection dominated($f = 1$), and gas pressure dominated ($\beta = 1$, so that $\gamma_{\rm equ} = 5/3$), as shown in Figure 3. The slim disk model is treated as advection dominated($f = 1$), and radiation pressure dominated ($\beta = 0$, so that $\gamma_{\rm equ} = 4/3$), as shown in Figure 4. The other two parameters are all set as $\alpha = 0.1$ and $n = 1.3$. In each figure, we show the function curves of $v_r(\theta)$, $v_\theta(\theta)$, $v_\phi(\theta)$, $p(\theta)$, $\rho(\theta)$ and the Mach numbers of v_r and v_θ, in which the adiabatic sound speed is calculated as

$$c_s = \sqrt{\gamma \frac{p}{\rho}}. \tag{24}$$

As shown in Equations (7-11), all the velocities scale with $\sqrt{GM/r}$. The density $\rho(\theta)$ is scaled

to 1 in the equatorial plane and it can be determined in a real case once the accretion rate at a certain radius is given. The pressure p is also scaled, and it satisfies the relation that $p(\theta)/\rho(\theta) = (p/\rho)/(GM/r)$. So once we get the actual density ρ at a certain radius, we can calculate the corresponding pressure p easily. The Mach number curves for v_r first decreases with θ, reaching 0 at some inclination, and then increases. That is because it changes sign along θ and we use absolute values in calculating the Mach numbers.

There are several common features among Figures 1-4. The value of v_θ is always non-positive. The value of v_r is always negative close to the equatorial plane, and becomes positive at smaller inclinations. In each of these figures, there exists a certain inclination θ_0 at which $v_r(\theta) = 0$. This θ_0 has similar meaning with the 'θ_0' in XW05, except that it is obtained through calculation rather than being preset as an input parameter in XW05. In the region $\theta_0 \leqslant \theta \leqslant 90^o$, $v_r(\theta)$ is negative, meaning that the accretion flow is moving towards the central accretor as inflow. So this region corresponds to the 'normal' accretion disk part in basic models and we call it the inflow region in this paper. In the region $\theta_b < \theta < \theta_0$, $v_r(\theta)$ is positive and the accretion flow is moving away from the central accretor, and we call this region the outflow region. The region between the upper boundary and the vertical axis contains the outflow which blows out of the upper boundary in the form of wind as shown in Figure 5, and we call this region the wind region, to distinguish it from the outflow region. It should be noted that our solutions actually cannot describe the structure of the wind region. However, it is natural to suppose that the flow structure in the wind region with $0 \leqslant \theta < \theta_b$ is also outflow, and the outflow region ($\theta_b < \theta < \theta_0$) can either be regarded as a transition region between inflow and outflow, or as part of the outflow which can still be described with the self-similar assumptions.

The physical properties shown in Figures 1 & 2 agree quite well with the SSD model. The rotation is very close to being Keplerian; the radial velocity is much smaller than the azimuthal velocity; and the disk is geometrically thin. However, as mentioned above, our calculation shows that even in the SSD case, there exists outflow in the accretion disk. As shown in Figures 5(a) & 5(b), this outflow is in the form of wind blowing out from the disk surface. Both v_r and v_θ are subsonic in the SSD cases.

The advection dominated solutions, as shown in Figures 3 & 4, are geometrically much thicker than the solutions with low advection, and are able to describe the structure of the majority of the space, except only a small region near the vertical axis. The rotation is sub-Keplerian and the radial velocity can be comparable with the azimuthal velocity. Both the ADAF and the slim disk case show strong outflows compared with the SSD cases, which can be seen more clearly in Figure 5. v_θ keeps to be subsonic for both cases. However, for the slim disk case (Figure 4), v_r becomes supersonic near the vertical axis, displaying a stronger outflow than the other three typical solutions.

Outflow is the result of the competition among the pressure gradient, the centrifugal force and the gravitational force. As we have mentioned before, the key feature of the outflow in our work is positive v_r, so we would like to investigate the properties of these forces along the radial direction. The radial components of the pressure gradient, the centrifugal force and the gravitational force can be written respectively as

$$-\frac{1}{\rho}\frac{\partial p}{\partial r} = A(\theta)\frac{GM}{r^2}, \tag{25}$$

$$\frac{v_\phi^2}{r} = B(\theta)\frac{GM}{r^2}, \tag{26}$$

$$\frac{GM}{r^2} = 1\cdot\frac{GM}{r^2}, \tag{27}$$

in which

$$A(\theta) = (1+n)\frac{p(\theta)}{\rho(\theta)} \tag{28}$$

$$B(\theta) = v_\phi^2(\theta). \tag{29}$$

We plot the values of $A(\theta)$, $B(\theta)$ and $A(\theta)+B(\theta)$ for the four typical solutions in Figure 6. The dotted lines correspond to the gravitational force which is scaled as 1; the dashed lines correspond to the radial component of the centrifugal force; the dot-dashed lines correspond to the radial component of the pressure gradient; and the solid lines correspond to the sum of the radial components of the centrifugal force and the pressure gradient, which drives the outflow. Figure 6(a) shows the properties of gas pressure dominated SSDs, while Figure 6(b) shows the properties of radiation pressure dominated SSDs. It can be seen that for both of the SSD cases, the influence of pressure gradient is very small, and almost in the entire range of the solution, the gravitational force is balanced with the sum of the centrifugal force and the pressure gradient in the radial direction. This is consistent with the SSD model in which both the advection and the pressure gradient are small enough to be neglected. Therefore these two solutions have similar accretion flow structure and only some quantitative differences exist between each other.

On the other hand, for the advection dominated cases, such as the ADAF case (Figure 6(c)) and the slim disk case (Figure 6(d)), the pressure gradient plays a more important role than the centrifugal force and drives a significant outflow as θ decreases. The slim disk case has qualitative differences from the other three cases. In both SSD cases and the ADAF case, the radial component of pressure gradient starts decreasing at smaller inclination angle, and to balance this effect, the disk rotates faster as θ decreases to increase the centrifugal force, as shown in Figures 1-3. However in the slim disk case, the radial component of the pressure gradient keeps increasing as θ decreases. It not only drives a much stronger outflow than the other three cases, but also reduces the required centripetal force to keep the disk rotating. Thus the disk rotates slower as θ decreases, as shown in Figure 4.

As a comparison with NY95, we also present here a solution with parameters $\alpha = 0.1$, $n = 3/2$, $\gamma_{\rm equ} = 1.6061$ and $f = 1$ in Figure 7. This set of parameters corresponds to '$\epsilon\prime = 0.1$' in NY95. In this case, the accretion flow doesn't contain outflow and the three components of velocity and the sound speed remain constant in the structure. The curves of $\rho(\theta)$ and $v_r(\theta)$ don't agree well with NY95, however this is because NY95 also sets the boundary conditions on the vertical axis and the values of $\rho(\theta)$ and $v_r(\theta)$ are limited by these boundary conditions. Our solution only uses the boundary conditions in the equatorial plane, and can still reach the vertical axis in this case and has a reasonable distribution of physical properties, which further proves the applicability of our method.

3.2. Solution Dependence on Input Parameters

In this section we show how the solutions change according to different input parameters respectively, and discuss their physical meanings. As shown in §3.1, the whole space is generally divided into three regions: an inflow region, an outflow region and a wind region. As the accretion flow is symmetrical both axially and under reflection in the equatorial plane, we only need to investigate the flow structure in a quadrant of the $r\theta$ plane. In this case, the inflow region starts from the equatorial plane ($\theta = 90^{\rm o}$) to the inclination $\theta = \theta_0$ where $v_r(\theta) = 0$; the outflow region starts from the inclination $\theta = \theta_0$ to the upper boundary of the flow structure at $\theta = \theta_{\rm b}$, and beyond that is the wind region ($0 < \theta < \theta_{\rm b}$) in which the motion of the matter doesn't satisfy the self-similar assumptions. Here we use θ_0 and $\theta_{\rm b}$ as indicators of the disk size in θ-direction, which directly reflects the size of the inflow region and the whole inflow/outflow region, respectively. In the figures showing how the properties of solutions change according to input parameters, each line represents a set of solutions, and we assign a unique label for each solution set for clarity. Table 1 lists all the solution set labels, their input parameters and corresponding lines at the end of §3.2.

1) Solution dependence on α

The dependence of θ_0 and $\theta_{\rm b}$ on α is shown in Figure 8. First we can clearly see that over a large range of α, the advection dominated solutions have both larger inflow region and larger inflow/outflow region. That's because in these solutions most of the viscous heating is stored in the accretion flow as internal energy, resulting in larger pressure at given density and thus larger size of the whole inflow/outflow region.

For solutions with the same advective factor f, gas pressure dominated solutions generally have larger inflow region. The inflow region lasts from the equatorial plane to the inclination θ_0 where v_r reaches 0, so its size depends on the behavior of v_r. In the equatorial plane, the reflection

symmetry gives Equation (21), and when it is substituted into Equations (17), (19) & (20), we can get

$$2(n+1)\frac{p(\theta)}{\rho(\theta)} + v_r^2(\theta) + 2(v_\phi^2(\theta) - 1) = 0, \quad (30)$$

$$-2(n-2)\alpha\frac{p(\theta)}{\rho(\theta)} + v_r(\theta)v_\phi(\theta) = 0, \quad (31)$$

$$2(n\gamma_{\rm equ} - n - 1)v_r(\theta) - 3\alpha f(\gamma_{\rm equ} - 1)v_\phi(\theta) = 0. \quad (32)$$

Equation (30) describes the hydrodynamical balance in the radial direction among the pressure gradient, the centrifugal force and the gravitational force, which determines the acceleration of v_r (the term $v_r^2(\theta)$ represents the acceleration of v_r under the self-similar assumptions). Equation (31) describes how the viscosity affects the angular momentum transfer rate in the equatorial plane. Equation (32) describes the energy mechanism of the accretion flow that a fraction f of the dissipated energy is advected as stored entropy. It should be noted that v_r is generally negative in the equatorial plane, so the absolute value of v_r can be written as (according to Equation (32))

$$|v_r(90^{\rm o})| = -v_r(90^{\rm o}) = \frac{3\alpha f}{2n}v_\phi(90^{\rm o})\left[\frac{1}{1 - n(\gamma_{\rm equ} - 1)} - 1\right]. \quad (33)$$

If $v_\phi(90^{\rm o})$ remains the same, then in the range of parameters we study in this paper, $|v_r(90^{\rm o})|$ increases with $\gamma_{\rm equ}$. However $v_\phi(90^{\rm o})$ also changes with input parameters, and the exact value of $v_r(90^{\rm o})$ should be calculated via Equations (30)-(32). Figure 10 shows the profile of $v_r(90^{\rm o})$ vs $\gamma_{\rm equ}$ when other parameters are taken as $n = 1.3$ and $\alpha = 0.1$. It can be seen that for both the advection dominated solutions and the solutions with little advection, $|v_r(90^{\rm o})|$ increases with $\gamma_{\rm equ}$. With a larger value of v_r in the equatorial plane, the accretion flow is inclined to undergo a larger range of θ to change v_r to 0, resulting in a larger inflow region. For the two SSD cases, as their flow structures are quite similar, larger values of v_r in the equatorial plane give the gas pressure dominated solution set a_1 larger inflow regions than a_2. For the advection-dominated cases, not only the equatorial value of v_r is smaller in the slim disk case than that in the ADAF case, but its radial direction pressure gradient also increases as θ decreases, giving a larger outward acceleration to v_r, thus the gas pressure dominated solutions a_3 have larger inflow regions than the radiation pressure dominated solutions a_4.

The solution set a_4, which corresponds to the slim disk model, has a large outflow size over a broad range of α, displaying a large outflow area. The solutions corresponding to the SSD model, a_1 and a_2, have very small outflow regions, and their outflows are mainly in the form of wind blowing out of the disk surface instead of escaping in the outflow region. The solution set a_3, which corresponds to the ADAF model, has a moderate outflow region with small α. However as α increases, this outflow region quickly disappears and the outflow takes the form of wind blowing out of the upper surface. The velocity field displayed in Figure 5 is an example for $\alpha = 0.1$.

α is connected with both the viscous heating and the angular momentum transport of the accretion flow. Larger α will increase the viscous heating for a fixed surface density. But at the same time it also increases the angular momentum transfer rate, thus increasing v_r and decreasing surface density, which decreases the total viscous heating rate. Therefore the dependence of the viscous heating rate on α, is somewhat complex. Viscous heating represents how much gravitational energy is converted to internal energy. But some of it is lost due to radiation and eventually there is only an f fraction of the viscous heating which is converted to internal energy. The increase in the internal energy will raise the temperature and subsequently the pressure, thus increasing the size of the accretion flow. However, for the SSD cases shown in a_1 & a_2, f is very small, thus the energy converted to internal energy is negligible and the disk structure is dominated dynamically by the gravity and the rotation of the material, rather than the pressure gradient. As a result, the sizes of accretion flows change very little with different α for a_1 & a_2.

On the other hand, for the advection dominated solutions a_3 & a_4, a large fraction of the gravitational energy is eventually stored as internal energy, so that the pressure gradient plays a more important role in determining the flow structure as mentioned in §3.1. Therefore the sizes of accretion flows are closely connected with α. In Figure 8 we can see that for a_3 & a_4, when α is very small, the viscous process is not quite effective, therefore both the inflow region size and the outflow region size are small (it's easy to understand if we consider the situation $\alpha = 0$, in which case no accretion flow will be formed). From this small value, along with the increasing of α, the viscous process starts to take effect and the whole inflow/outflow region size starts to increase, until it reaches a maximum size at $\alpha \sim 0.05$ for line a_3' and $\alpha \sim 0.12$ for line a_4'(the exact value of α for maximum size also depends on other parameters). From then on, the larger values of v_r starts to dominate the total effect and the corresponding accretion flow size starts to decrease. This property can also be seen in the top left panel of Figure 17, which displays the ratio of the outflow rate to the inflow rate.

It should be noted that, in Figure 8, the size change based on α is different between the whole inflow/outflow region and the pure inflow region. The size of the whole inflow/outflow region decreases after a peak at a certain α while the size of the pure inflow region keeps increasing. For solution sets a_1, a_3 and a_4, this difference is enough to generate a critical α_c respectively, at which the outflow region totally disappears. So for $\alpha > \alpha_c$, the accretion flow that we can resolve with self-similar assumptions is composed of pure inflow and we didn't find a surface at which $v_r(\theta_0) = 0$. That's why we say that the assumption used in XW05 may not be true for large α. Kluzniak and Kita (2000) also found this critical α which was calculated to be $\sqrt{15/32} \approx 0.685$ by them. In our work, however, α_c depends on other parameters and can change significantly, as shown in Figure 8 (~ 0.96 for a_1, ~ 0.24 for a_3 and ~ 0.74 for a_4). For a_2, this α_c is above 1 and it's not displayed.

Figures 9 displays the v_r distribution along the θ-direction for solutions with different α. Figures (a), (b), (c) and (d) correspond to the four sets of solutions in Figure 8 respectively, and the solid, dashed and dotted lines correspond to different α as indicated in the legends. The range of the axes are adjusted to show more details in comparison. We can see that in the solutions corresponding to the SSD model, i.e. Figures 9(a) & 9(b), v_r is almost proportional to α. That is because when alpha increases, so does the angular momentum transfer rate. For the SSD case, the accretion flow structure is mostly determined by gravity and rotation as discussed in §3.1, and the rotation is quasi-Keplerian, so the increase in angular momentum transfer rate increases v_r almost proportionally. A special case in the equatorial plane is shown by Equation (31), in which when v_ϕ is Keplerian, the value of v_r is proportional to α. For the ADAF and the slim disk cases, because pressure gradient plays an important role in the accretion flow structure, v_r is generally not proportional to α, but still positively correlated with α as shown in Figure 9(c) & 9(d). We can also see that some lines in Figure 9 don't contain positive v_r. That's because the α values for these solutions are greater than the critical value α_c mentioned above.

2) Solution dependence on n

The parameter n describes how the density changes along the radius in our self-similar assumptions. As discussed in §3.1, when $n = 3/2$, the entire flow structure can be described by the same set of self-similar solutions, but doesn't contain outflow; when $n < 3/2$, the solution contains outflow but the self-similar assumptions cannot be applied to the region near the vertical axis; solutions with $n > 3/2$ are unlikely to happen in real cases.

The dependence of θ_0 and θ_b on n is shown in Figure 11. Figures 12 & 13 display the v_r and v_θ distributions along the θ-direction for solutions with different n. We can see that solutions all achieve a maximum size at $n = 3/2$ for both the whole inflow/outflow region and the inflow only region. This is because when $n = 3/2$ the entire space can be described by the same set of self-similar equations as discussed in §3.1. In this case, $v_\theta = 0$ and mass is conserved on the streamlines pointing exactly at the central accretor, thus no outflow is required. Before reaching the maximum value at $n = 3/2$, the flow size is positively correlated with n as a general trend. As n decreases, according to Equation (22) $\dot{M}_{\rm eff}$ decreases faster inwards, which means a larger mass loss rate into the area beyond θ_b, resulting in the increase in the size of the wind region and the decrease in the size of the whole inflow/outflow region in Figure 11, and the increase in v_θ in Figure 13.

In Figure 11 line b_4' has 2 peaks. According to Equation (25), the radial pressure gradient is proportional to $(1+n)p/\rho$, so when p/ρ doesn't change much, the radial pressure gradient increases with n. In advection-dominated solutions b_3 & b_4, the radial pressure gradient is more important than centrifugal force in accelerating v_r, so for larger n which is inclined to have larger radial pressure gradient, one would expect to see faster increase in v_r and stronger outflow in the outflow region. These features of v_r can be seen in Figure 12. The radial pressure gradient is dominant

in the slim disk case as mentioned in §3.1, so the acceleration of v_r increases significantly with increasing n in the slim disk case, which can be seen in Figure 12(d) with a much steeper profile of v_r when $n = 1.3$. This increased outflow velocity in the outflow region can cause a steeper density drop along θ direction towards the upper boundary and therefore make the outflow region become smaller, creating a valley in line b_4' around $n = 1.4$.

The top right panel in Figure 17 shows how the ratio of the outflow rate to the inflow rate changes depending on n. We can see that when n becomes small enough, the ratio changes very little with n. In this range of n, the size of different regions also doesn't change much in Figure 10, and the flow structure is similar to each other.

For $\gamma_{\rm equ} = 5/3$, we cannot get a reasonable set of equatorial values for physical properties when n is larger than 3/2. For $\gamma_{\rm equ} = 4/3$, i.e. solutions b_2 and b_4, we can still get reasonable values of equatorial physical properties when n is larger than 3/2, so that we can calculate solutions with $n > 3/2$ in this case. Solutions with $n > 3/2$ have an effective accretion rate $\dot{M}_{\rm eff}$ that increases towards the central accretor, which implies that there must be matter injection into the accretion flow from high latitudes. This kind of matter injection is not likely to happen in real cases, so we won't pay more attention to the solutions with $n > 3/2$ here. Solutions with $n = 3/2$ and $n < 3/2$ both exist and have quite different structure. However, as in NY95, solutions with $n = 3/2$ are only for ADAFs, while solutions with $n < 3/2$ in our work is applicable to a much wider range of accretion disks. In this sense, we believe that outflows should be common in various accretion disks.

3) Solution dependence on f

The dependence of θ_0 and $\theta_{\rm b}$ on f is shown in Figure 14. It has already been discussed that as the advective factor f increases, the size of the whole inflow/outflow region also increases, which is shown more clearly here in Figure 14. The gas pressure dominated solutions have larger inflow region in agreement with Figures 8 & 11, and the reason has been discussed in §3.2.1.

As f increases, the size of the outflow region increases faster for radiation pressure dominated flows, displaying a larger outflow size for solutions corresponding to the slim disk model. The reason is that, as f increases, a larger fraction of viscous heating is converted to internal energy instead of being lost via radiation, raising the temperature of the accretion flow. The gas pressure is proportional to T while the radiation pressure is proportional to T^4, so in the radiation pressure dominated solutions, p increases faster as f increases. The increased pressure inflates the outflow region and causes a stronger outflow. On the other hand, as f gets close to 1, eventually the outflow velocity at small inclination becomes so large, that it will instead reduce the size of the outflow region because the material lost in the outflow region is limited. As shown in the bottom left panel of Figure 17, at a certain $f \sim 0.9$, the fraction of material lost in the outflow region

reaches an upper limit, and with larger f, this fraction almost remains unchanged. In this range of f, the larger outflow velocity will instead shrink the size of the outflow region. This causes line c_2' in Figure 14 to reach a peak of $\sim 90^o$ at $f \sim 0.9$ (corresponding to Figure 17(c)), and to start decreasing as f becomes larger.

4) Solution dependence on $\gamma_{\rm equ}$ (and consequently β)

The dependence of θ_0 and $\theta_{\rm b}$ on $\gamma_{\rm equ}$ is shown in Figure 15. The top axis displays the corresponding values of β when γ takes the value of 5/3. If the intrinsic heat capacity ratio is not 5/3 (e.g. when dealing with proto-stellar accretion disks with unionized gas), the corresponding β in Figure 15 may not be correct, but one can still calculate the correct β with $\gamma_{\rm equ}$ and γ according to Equation (14). Figure 16 displays the v_r and v_θ distributions along the θ-direction for solutions with different $\gamma_{\rm equ}$. The bottom right panel of Figure 17 shows how the ratio of the outflow rate to the inflow rate changes depending on $\gamma_{\rm equ}$ (and consequently β).

In Figure 15, the size of the pure inflow region generally increases with $\gamma_{\rm equ}$ (and consequently β). As shown in Figure 10 & 16 and discussed in §3.2.1, solutions with larger $\gamma_{\rm equ}$ (and consequently larger gas pressure ratio β) have larger values of v_r in the equatorial plane. This effect combined with the acceleration properties of v_r, causes solutions with larger $\gamma_{\rm equ}$ (and consequently larger β) to have larger inflow region. For solutions with low advection, as the outflow region is very small, the size of the whole inflow/outflow region also displays similar profile with increasing $\gamma_{\rm equ}$ (and consequently β). That's why lines d_1, d_1' and d_2 all have positive slope in Figure 15.

In Figure 17(d), there exists a transition point for the advection dominated solutions, and for solutions with $\gamma_{\rm equ} \lesssim 3/2$ (corresponding to $\beta \lesssim 2/3$), the ratio of the outflow rate to the inflow rate keeps being large. As discussed before, for the advection dominated cases, radiation pressure dominated solutions have larger pressure gradient, shown as steeper velocity profiles in Figure 16, which drives stronger outflow. As shown in Figure 17(d), the outflow to inflow ratio increases as $\gamma_{\rm equ}$ decreases from 5/3 (which indicates the decreasing of gas pressure ratio β from 1). However, the outflow rate cannot exceed the inflow rate and eventually the increase will cease, reaching a transition point at $\gamma_{\rm equ} \sim 3/2$ (corresponding to $\beta \sim 2/3$). For $\gamma_{\rm equ} \lesssim 3/2$ (corresponding to $\beta \lesssim 2/3$), the outflow to inflow ratio remains almost unchanged. Further decrease in $\gamma_{\rm equ}$ will continue to increase the outflow velocity, while the fraction of the inflow lost in the outflow region is almost unchanged, so the size of the outflow region will shrink. This feature can be also seen in Figure 15, which shows that the size of the outflow region for advection dominated solutions first increases with decreasing $\gamma_{\rm equ}$, reaching an upper limit at $\gamma_{\rm equ} \sim 3/2$ (corresponding to $\beta \sim 2/3$), and decreases with decreasing $\gamma_{\rm equ}$ after that. It should be noted that, this transition value of $\gamma_{\rm equ}$ depends on other input parameters, and this value of $\sim 3/2$ corresponds to $\alpha = 0.1$, $n = 1.3$ and $f = 1$. For the solutions with low advection, the ratio of the outflow rate to the inflow rate don't change much and are always very small as shown in Figure 17(d).

5) Bends in solutions

We have shown the solution dependence on different input parameters. The solutions sometimes show bends which we would like to discuss more specifically here.

The bend about α is closely connected with the energy mechanism. As discussed in §3.2.1, the dependence of viscous heating on α is somewhat complex. It has a peak at a certain value of α (which depends on other input parameters), and decreases on both sides. For the advection dominated solutions a_3 & a_4, most of the viscous heating is stored as internal energy in the accretion flow, which raises the temperature and subsequently the pressure, thus increasing the size of the accretion flow. On the other hand, the increase in α also increases the absolute value of v_r of the inflow near the equatorial plane, in which case more work needs to be done to drive an outflow, decreasing the outflow region as α increases. So naturally the size of the whole inflow/outflow region also has a peak at some value of α. As α increases from a very small value, at first the increase in viscous heating dominates the total effect, and the size of the accretion flow increases, until it reaches a maximum value; from then on, the increase in v_r starts to dominate the total effect, which makes the outflow more difficult to produce and also reduces viscous heating when α becomes large enough, thus shrinking the size of the whole accretion flow. To show the energy profile for solutions with different α, here we calculate the θ-averaged Bernoulli function $\overline{Be}$. The Bernoulli function represents the specific total energy in the accretion flow. A positive value of the Bernoulli function is only a necessary, not a sufficient, condition for outflow formation (Abramowicz et al. 2000). However, as our solutions have already showed outflow structure in the velocity fields, a larger value of the Bernoulli function indicates that the accretion flow is more likely to contain stronger outflow. Locally the Bernoulli function can be written as

$$Be = W + \frac{1}{2}V^2 + \Phi = e + \frac{p}{\rho} + \frac{1}{2}V^2 + \Phi = \frac{GM}{r}\left[\frac{1}{2}(v_r^2(\theta) + v_\theta^2(\theta) + v_\phi^2(\theta)) + \frac{\gamma_{\rm equ}}{\gamma_{\rm equ}-1}\frac{p(\theta)}{\rho\theta} - 1\right], \quad (34)$$

in which W is the specific enthalpy, V is the velocity (all three components included) and Φ is the gravitational potential. So the θ-averaged Bernoulli function can be written as

$$\begin{aligned}\overline{Be} &= \frac{\int_{\theta_{\rm b}}^{90^{\rm o}} \rho(\theta)\cdot Be\cdot 2\pi r^2\sin\theta dr\cdot(\pi/180^{\rm o})d\theta}{\int_{\theta_{\rm b}}^{90^{\rm o}} \rho(\theta)\cdot 2\pi r^2\sin\theta dr\cdot(\pi/180^{\rm o})d\theta} \\ &= \frac{GM}{r}\frac{\int_{\theta_{\rm b}}^{90^{\rm o}} \rho(\theta)\cdot\left[\frac{1}{2}(v_r^2(\theta)+v_\theta^2(\theta)+v_\phi^2(\theta)) + \frac{\gamma_{\rm equ}}{\gamma_{\rm equ}-1}\frac{p(\theta)}{\rho\theta} - 1\right]\sin\theta d\theta}{\int_{\theta_{\rm b}}^{90^{\rm o}} \rho(\theta)\cdot\sin\theta d\theta}. \end{aligned} \quad (35)$$

Figure 18 displays how the θ-averaged Bernoulli function $\overline{Be}$ changes with variant α for the advection dominated cases. It can be seen that the positions of the peaks agree quite well with the bends of line a_3' and line a_4' in Figure 8.

Figure 19 displays the velocity fields of solutions around the bend for variant α. The values of α are chosen so that the solutions on both sides of the peaks have similar upper boundaries ($\sim 10^o$). It can be seen that the velocities in the outflow region are more aligned to the θ direction in the right panel of each row than those in the left panel. That's because larger α increases the angular momentum transfer rate, thus increases the absolute value of v_r near the equatorial plane where most of the material is accreted. The value of v_r is negative in the equatorial plane and changes gradually to positive values in the outflow region under the effect of pressure gradient and centrifugal force. The absolute value of v_r in the equatorial plane in the right panel of each row is significantly larger than that in the left panel, so when pressure gradient doesn't differ much, the positive values of v_r in the outflow region will be smaller for larger α and the velocities will be more aligned to the θ direction. The solutions corresponding to slim disks (the second row) show velocities more aligned to the radial direction in the outflow region than those corresponding to ADAFs (the first row), due to larger pressure gradient and thus larger values of v_r in the outflow region.

The bends in solution dependence on n, f and $\gamma_{\rm equ}$ have different physical mechanism from that on α. It has been mentioned that, as n increases, f increases or $\gamma_{\rm equ}$ decreases, the pressure gradient increases and drives stronger outflow. However, the outflow rate cannot exceed the inflow rate. At seen in Figure 17, the ratio of the outflow rate to the inflow rate for lines b_4, c_2 and d_2 will eventually reach an upper limit at certain values of corresponding parameters. For solution sets c_2 and d_2, further increase in f or further decrease in $\gamma_{\rm equ}$ will continue to increase the radial outflow velocity, while the outflow rate in the outflow region is almost unchanged, so the size of the outflow region will shrink. For the solution dependence on n, the bend near $n = 1.25$ has similar physical reason as the bends for f and $\gamma_{\rm equ}$. However, the size of the accretion flow has another peak at $n = 3/2$, where the flow is always radial (with rotation) and no outflow is needed. So line b_4 in Figure 17 starts to drop as n gets close to 3/2 and line b_4' in Figure 11 gets to another peak at $n = 3/2$.

Figure 20 displays the velocity fields of solutions around the bend for variant n, f and $\gamma_{\rm equ}$. It can be seen that, as n increases (the first row), f increases (the second row) or $\gamma_{\rm equ}$ decreases (the third row), the flow patterns display similar evolvement for these parameters: at first both the accretion flow size and the radial outflow velocity increase; after the corresponding parameter gets past the respective value at the transition point (the middle panels in all three rows of Figure 20), the radial outflow velocity continues to increase while the size of the accretion flow decreases. The velocities in the outflow regions become more aligned to the radial direction from left to right in all three rows, due to increased radial outflow velocities.

The labels for solution sets and lines which appear in the text and figures are summarized in Table 1 along with their corresponding input parameters.

TABLE 1
LABELS AND CORRESPONDING PARAMETERS

Label for solution set	Label for lines	α	n	f	$\gamma_{\rm equ}$
a_1	a_1, a_1'	0.01 - 1	1.3	0.01	5/3
a_2	a_2, a_2'	0.01 - 1	1.3	0.01	4/3
a_3	a_3, a_3'	0.01 - 1	1.3	1	5/3
a_4	a_4, a_4'	0.01 - 1	1.3	1	4/3
b_1	b_1, b_1'	0.1	0 - 1.5	0.01	5/3
b_2	b_2, b_2'	0.1	0 - 1.5	0.01	4/3
b_3	b_3, b_3'	0.1	0 - 1.5	1	5/3
b_4	b_4, b_4'	0.1	0 - 1.5	1	4/3
c_1	c_1, c_1'	0.1	1.3	0.01 - 1	5/3
c_2	c_2, c_2'	0.1	1.3	0.01 - 1	4/3
d_1	d_1, d_1'	0.1	1.3	0.01	4/3 - 5/3
d_2	d_2, d_2'	0.1	1.3	1	4/3 - 5/3

4. SUMMARY AND DISCUSSION

With the self-similar assumptions along the radial direction and boundary conditions obtained from the reflection symmetry in the equatorial plane, we are able to solve the Navier-Stokes Equations along the θ direction explicitly, and the velocity field is obtained. The result shows that outflows are common in all kinds of accretion disk models, which is consistent with some numerical simulation works (e.g. Ohsuga et al.2005; Ohsuga & Mineshige 2007; Ohsuga et al. 2009). Generally the accretion flow consists of three different regions: an inflow region near the equatorial plane which contains the largest portion of mass, an outflow region above the inflow region in which the matter starts escaping the central accretor in the r-direction, and a wind region which contains the material blowing out from the boundary of the outflow region. The structure of the inflow and the outflow region can be resolved in our solutions, while the wind region doesn't obey the self-similar assumptions and can not be resolved by our calculation. The inflow region and the wind region are essential to form a steady accretion flow structure. The outflow region is missing in the cases with large viscosity parameter $\alpha > \alpha_{\rm c}$. The critical value $\alpha_{\rm c}$ depends on other parameters and is ~ 0.24 for ADAFs, ~ 0.74 for slim disks and ~ 0.96 for gas pressure dominated SSDs when $n = 1.3$.

To compare with the popular analytical models, we calculated solutions with parameters corresponding to the SSD, the ADAF and the slim disk models. The solutions corresponding to the SSD model have relatively thin, quasi-Keplerian disks with very small outflow regions, and the outflows mostly take the form of wind from the disk surface. The solutions corresponding to the ADAF and slim disk models have thick, sub-Keplerian disks. The solution corresponding to the

ADAF model has a moderate outflow region which shrinks quickly with the increase of α, and the outflow mainly takes the form of wind. However as the upper boundary of the outflow region is close to the vertical axis, eventually the outflow may take the form of bipolar jets, though we cannot actually resolve the explicit structure around the vertical axis. The solutions corresponding to the slim disk model has a large outflow region in which most of the outflow takes place, and near the upper boundary of the outflow region, the material escapes with supersonic velocity.

Our calculation displays very small outflow regions for input parameters corresponding to the SSD model, and for these solutions the inflow region has similar structure with the one-dimensional SSD model. However the accretion rate inside the disk may not be conserved along the radius due to mass lost via wind. For the ADAF and the slim disk cases, our result displays an outflow region too large to be neglected, and we think it's necessary to consider the explicit structure in the θ or z direction to get more realistic results than the traditional analytical models. It was proposed in several works (Gu & Lu, 2007; Jiao et al. 2009) that the slim disk model has an upper limit of accretion rates, above which outflows seem to be inevitable. Later in another paper (Jiao & Lu 2009), one-dimensional steady transonic global solutions for slim disks with presumed amount of outflows were calculated, and in this case the proposed upper limit of accretion rates for slim disks can be exceeded. Another paper written by Takeuchi et al. (2009) used the outflow data from two-dimensional radiation-hydrodynamic (RHD) simulations to construct an one-dimensional steady solution, and the result shows that the emergent spectra do not sensitively depend on the amount of mass outflow. However, these models are still one-dimensional models and they only incorporated the mass loss effect of outflow into their models, so the results still remain debatable. We think that two-dimensional solutions considering the hydrodynamical processes and radiative transfer along both the radial and the θ direction are required to examine the topic, which we are planning to do in our future work.

We also investigated the dependence of the accretion flow structure on different input parameters respectively. f and $\gamma_{\rm equ}$ (consequently β) both have some transition values as discussed in §3.2.3 and §3.2.4, at which the outflow region reaches a maximum size. Generally when $f \gtrsim 0.9$ and $\beta \lesssim 2/3$ (for intrinsic $\gamma = 5/3$), the accretion flow will have a large outflow region and strong outflow, as the aforementioned solutions corresponding to the slim disk model. However, in what conditions the transition happens depends on other input parameters and it won't happen in case of large α due to the existence of the critical value $\alpha_{\rm c}$. Solutions with $n = 3/2$ don't contain outflow and they correspond to the solutions in NY95, which is only applicable to ADAFs. Solutions with $n < 3/2$ have the aforementioned three-region (or two-region for $\alpha > \alpha_{\rm c}$) structure. Solutions with $n > 3/2$ are not likely to happen in real cases.

Finally, we would like to mention some caveats in our work. The solutions obtained in this paper are steady solutions, and thus it is not guaranteed that they are stable solutions. These solu-

tions do not cover the whole space, so for the unresolved region near the axis, we know nothing about the detailed structure other than that it contains the material blowing out of the upper boundary in the form of wind. Our work is based on the simple αp prescription of viscosity, which is not bad according to recent MHD simulation works(Hirose et al. 2009; Ohsuga et al. 2009), especially when the flow is steady. However, it may be necessary to consider other components of the viscous stress tensor for solutions with large v_r. We also used the advective factor f to simplify the energy equation, and assumed f to be a constant. Realistically f should vary with both θ and r, which could be improved by considering the details of radiative transfer. We used Newtonian gravitational potential in our work, and it needs to be corrected when applied to study the structure close to the innermost stable circular orbit. In our calculation we didn't consider the effects of convection (e.g. Stone et al. 1999; Igumenshchev & Abramowicz 2000; Yuan & Bu 2010) or magnetic field (e.g. Blandford & Payne 1982; Naso & Miller 2010), which may be important in studying the accretion flow and the generation of outflows. Finally, it is necessary to abandon the self-similar assumptions if we want to investigate the disk and outflow structure more quantitatively and precisely. These caveats will be improved in our future work.

We thank Fu-Guo Xie for discussions and suggestions. We are also grateful to Marek Abramowicz, Feng Yuan, Wei-Min Gu and Li Xue for helpful comments. We also thank the referee for his/her constructive suggestions. This work was supported by the NSFC grant (No. 11033001) and the 973 program (No. 2007CB815405).

REFERENCES

Abramowicz, M. A., Chen, X., Kato, S., Lasota, J.-P., & Regev, O. 1995, ApJ, 438, L37

Abramowicz, M. A., Czerny, B., Lasota, J. P., & Szuszkiewicz, E. 1988, ApJ, 332, 646

Abramowicz, M. A., Lasota, J.-P., & Igumenshchev, I. V. 2000, MNRAS, 314, 775

Blandford, R. D., & Begelman, M. C. 1999, MNRAS, 303, L1

Blandford, R. D., & Begelman, M. C. 2004, MNRAS, 349, 68

Blandford, R. D., & Payne, D. G. 1982, MNRAS, 199, 883

Chartas, G., Brandt, W. N., & Gallagher, S. C. 2003, ApJ, 595, 85

Dotan, C., & Shaviv, N. J. 2010, arXiv:1004.1797

Fukue, J. 1989, PASJ, 41, 123

Fukue, J. 2004, PASJ, 56, 181

Gu, W.-M., & Lu, J.-F. 2007, ApJ, 660, 541

Hirose, S., Blaes, O., & Krolik, J. H. 2009, ApJ, 704, 781

Igumenshchev, I. V., & Abramowicz, M. A. 2000, ApJS, 130, 463

Jiao, C.-L., & Lu, J.-F. 2009, Chinese Physics Letters, 26, 049701

Jiao, C.-L., Xue, L., Gu, W.-M., & Lu, J.-F. 2009, ApJ, 693, 670

Kato, S., Fukue, J., & Mineshige, S. 2008, Black-Hole Accretion Disks: Towards a New Paradigm (Kyoto: Kyoto Univ. Press)

Kawabata, R., & Mineshige, S. 2009, PASJ, 61, 1135

King, A. R., Pringle, J. E., & Livio, M. 2007, MNRAS, 376, 1740

Kluzniak, W., & Kita, D. 2000, arXiv:astro-ph/0006266

Kusunose, M. 1991, ApJ, 370, 505

Loeb, A., Narayan, R., & Raymond, J. C. 2001, ApJ, 547, L151

Marrone, D. P., Moran, J. M., Zhao, J.-H., & Rao, R. 2006, ApJ, 640, 308

Narayan, R., & Yi, I. 1994, ApJ, 428, L13

Misra, R., & Taam, R. E. 2001, ApJ, 553, 978

Narayan, R., & Yi, I. 1995, ApJ, 444, 231

Naso, L., & Miller, J. C. 2010, A&A, 521, A31

Okuda, T., Teresi, V., Toscano, E., & Molteni, D. 2005, MNRAS, 357, 295

Ohsuga, K., Mori, M., Nakamoto, T., & Mineshige, S. 2005, ApJ, 628, 368

Ohsuga, K., & Mineshige, S. 2007, ApJ, 670, 1283

Ohsuga, K., Mineshige, S., Mori, M., & Kato, Y. 2009, PASJ, 61, L7

Sądowski, A., Abramowicz, M., Bursa, M., Kluźniak, W., Lasota, J.-P., & Różańska, A. 2011, A&A, 527, A17

Shakura, N. I., & Sunyaev, R. A. 1973, A&A, 24, 337

Stone, J. M., Pringle, J. E., & Begelman, M. C. 1999, MNRAS, 310, 1002

Takahara, F., Rosner, R., & Kusunose, M. 1989, ApJ, 346, 122

Takeuchi, S., Mineshige, S., & Ohsuga, K. 2009, PASJ, 61, 783

Xie, F.-G., & Yuan, F. 2008, ApJ, 681, 499

Xu, G., & Chen, X. 1997, ApJ, 489, L29

Xue, L., & Wang, J. 2005, ApJ, 623, 372

Yuan, F., & Bu, D.-F. 2010, MNRAS, 408, 1051

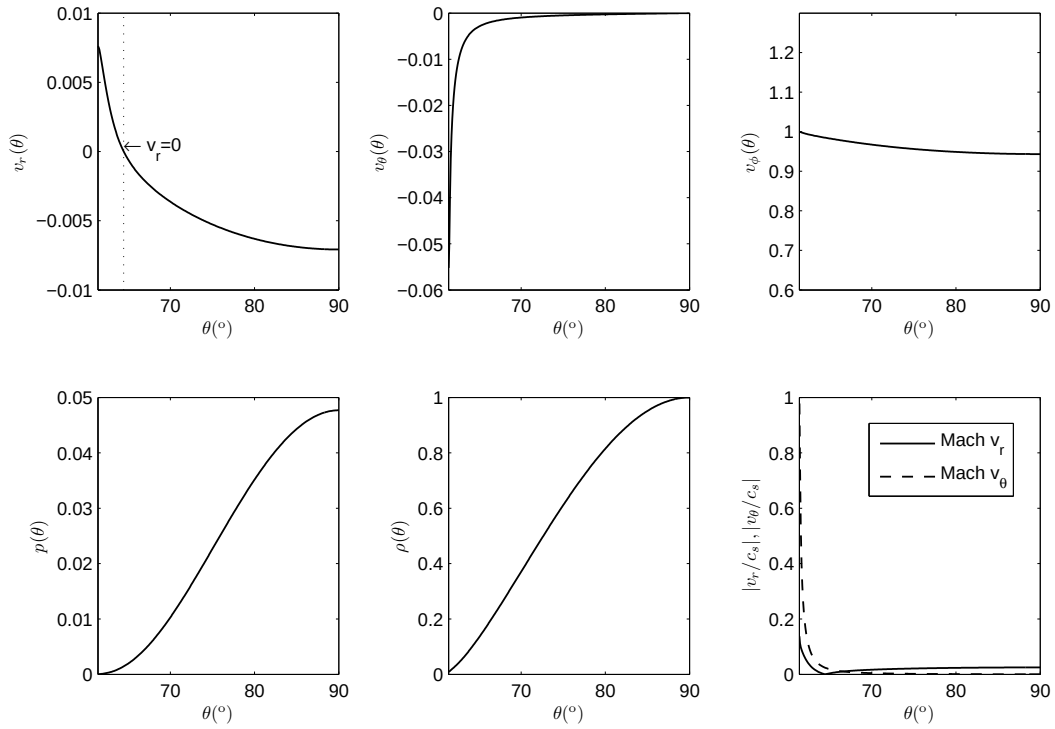

Fig. 1.— The solution corresponding to the gas pressure dominated region of the SSD model. Here $\alpha = 0.1$, $n = 1.3$, $f = 0.01$ and $\gamma_{\rm equ} = 5/3$, which correspond to gas pressure dominated monatomic ideal gas.

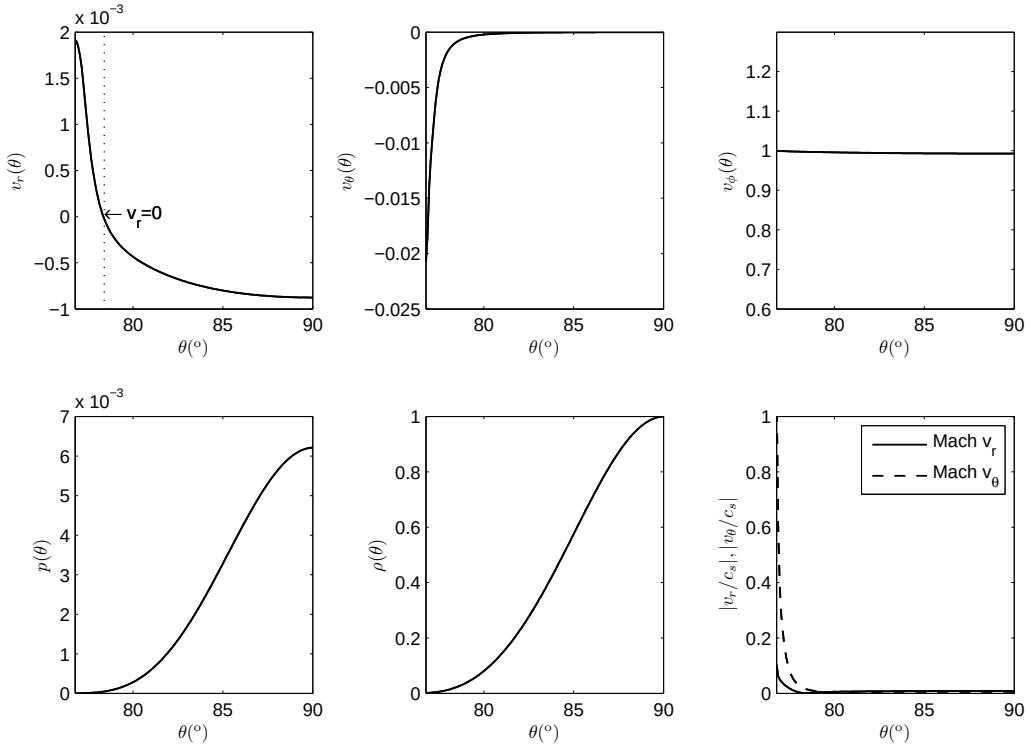

Fig. 2.— The solution corresponding to the radiation pressure dominated region of the SSD model. Here $\alpha = 0.1$, $n = 1.3$, $f = 0.01$ and $\gamma_{\rm equ} = 4/3$, which correspond to radiation pressure dominated monatomic ideal gas.

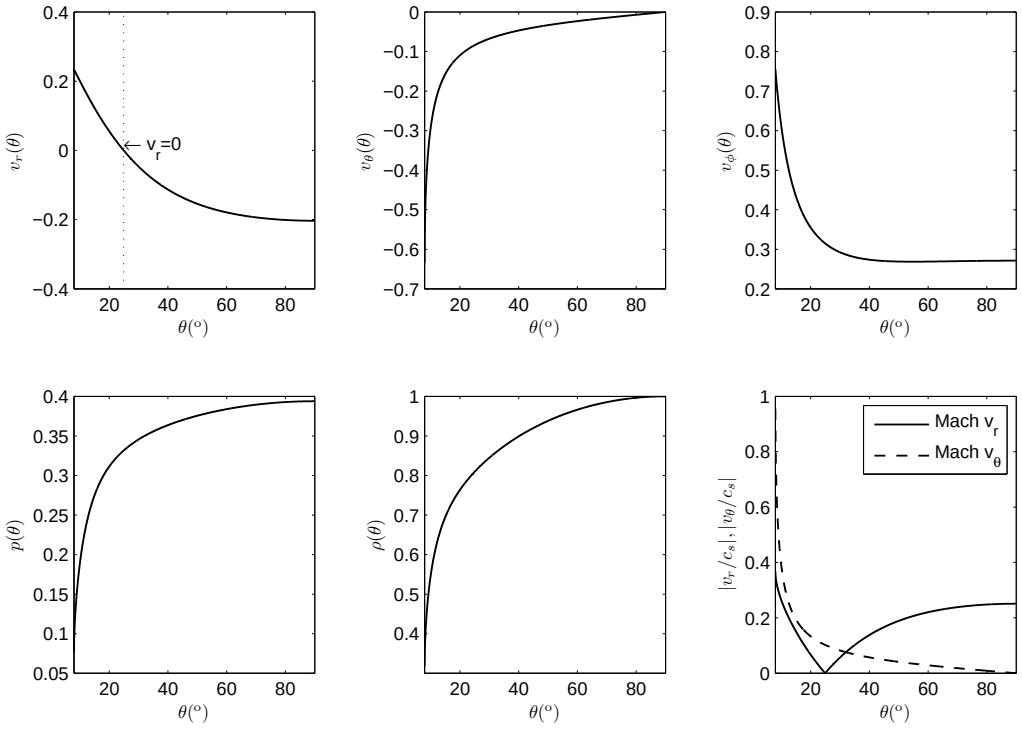

Fig. 3.— The solution corresponding to the ADAF model. Here $\alpha = 0.1$, $n = 1.3$, $f = 1$ and $\gamma_{\rm equ} = 5/3$, which correspond to gas pressure dominated monatomic ideal gas.

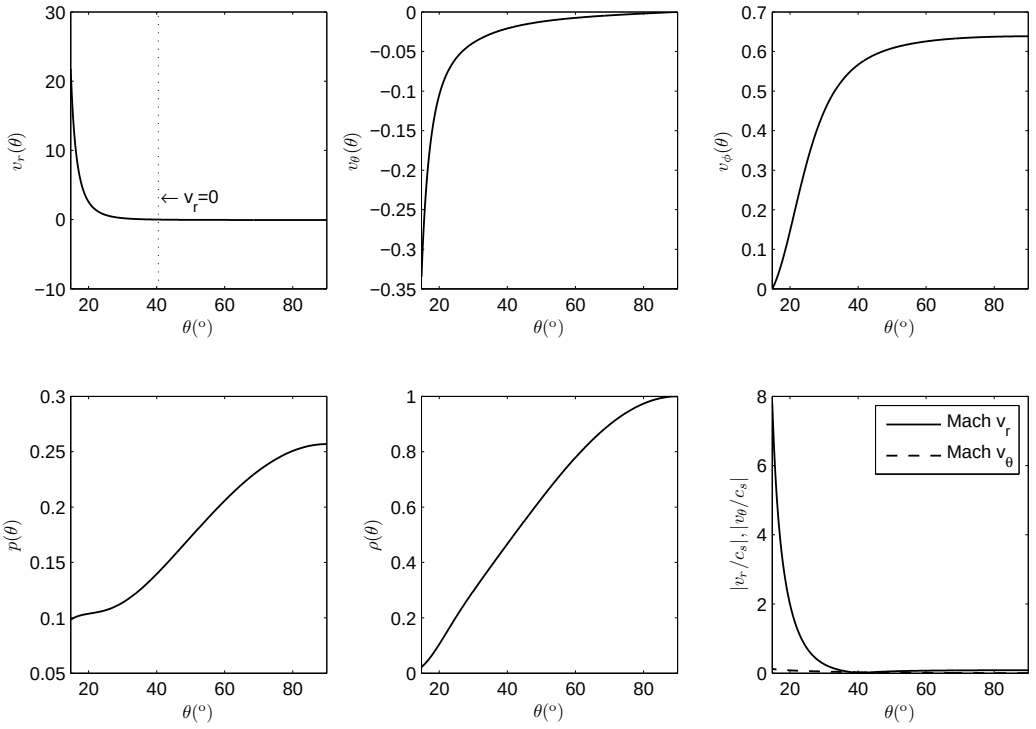

Fig. 4.— The solution corresponding to the slim disk model. Here $\alpha = 0.1$, $n = 1.3$, $f = 1$ and $\gamma_{\rm equ} = 4/3$, which correspond to radiation pressure dominated monatomic ideal gas.

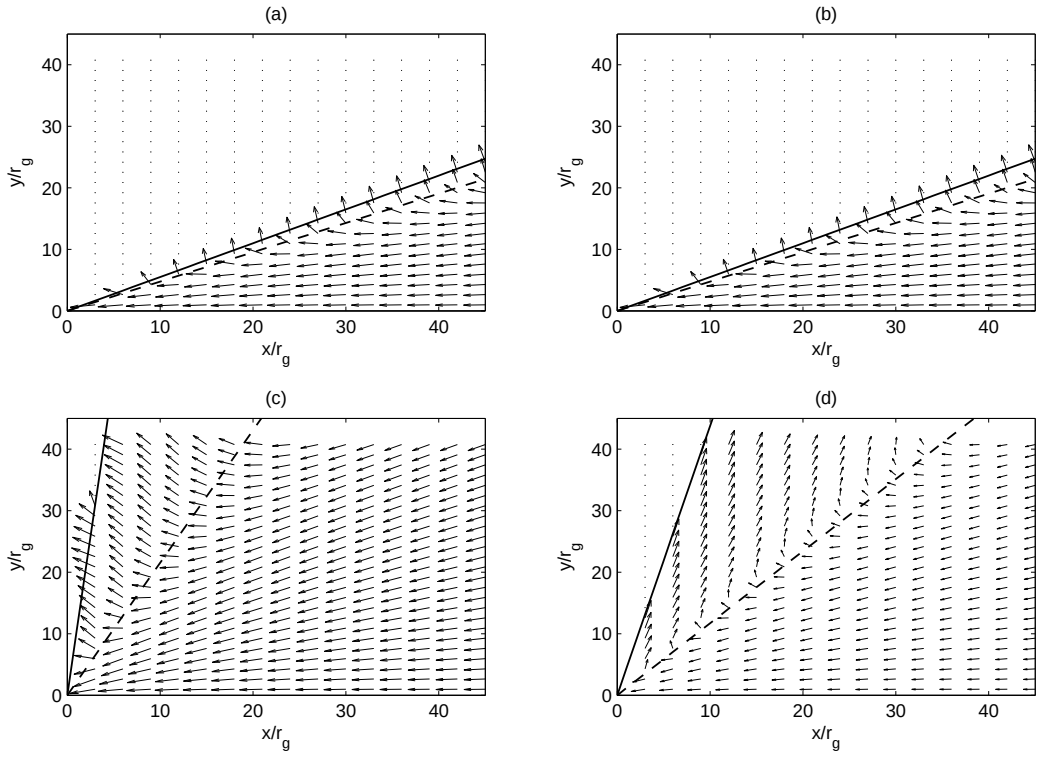

Fig. 5.— The velocity fields of the four typical solutions. Figures (a), (b), (c) and (d) correspond to input parameters of Figures 1-4 respectively. The lengths of arrows indicate the absolute values of the vector $\vec{v_r}(\theta)+\vec{v_\theta}(\theta)$, which are scaled logarithmically. The solid lines correspond to the inclination $\theta_{\rm b}$, while the dashed lines correspond to the inclination θ_0.

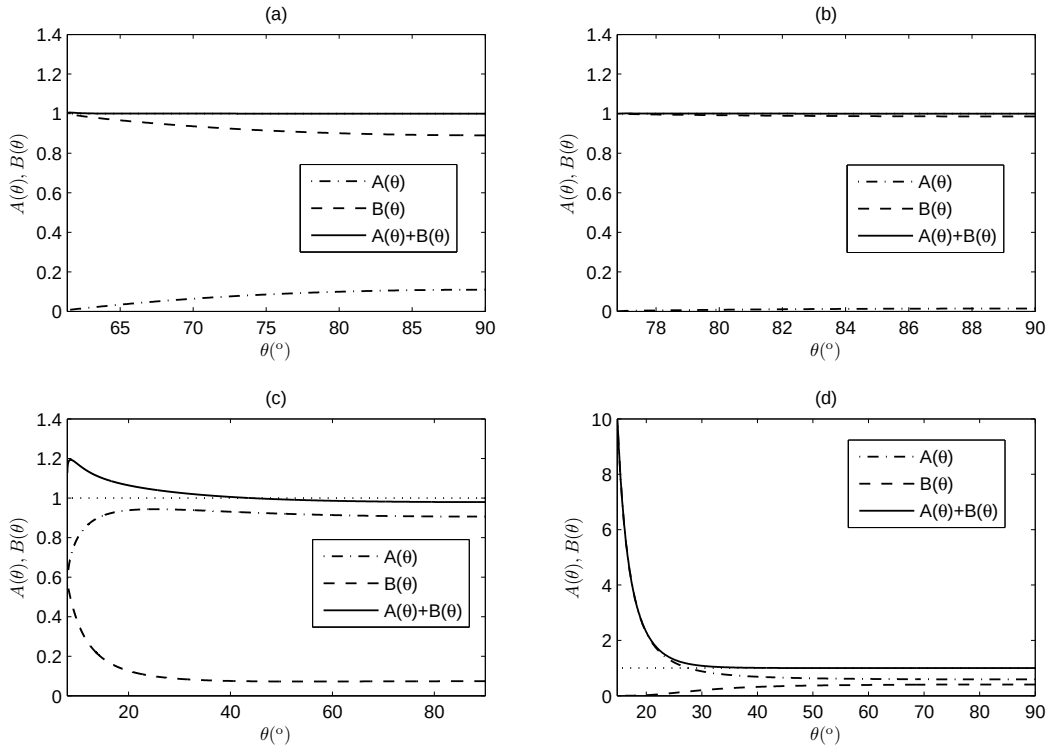

Fig. 6.— The radial components of the pressure gradient, the centrifugal force and the gravitational force for the four typical solutions. Figures (a), (b), (c) and (d) correspond to input parameters of Figures 1-4 respectively. The dotted lines correspond to the gravitational force which is scaled as 1; the dashed lines correspond to the radial component of the centrifugal force; the dot-dashed lines correspond to the radial component of the pressure gradient; and the solid lines correspond to the sum of the radial components of the centrifugal force and the pressure gradient, which drives the outflow.

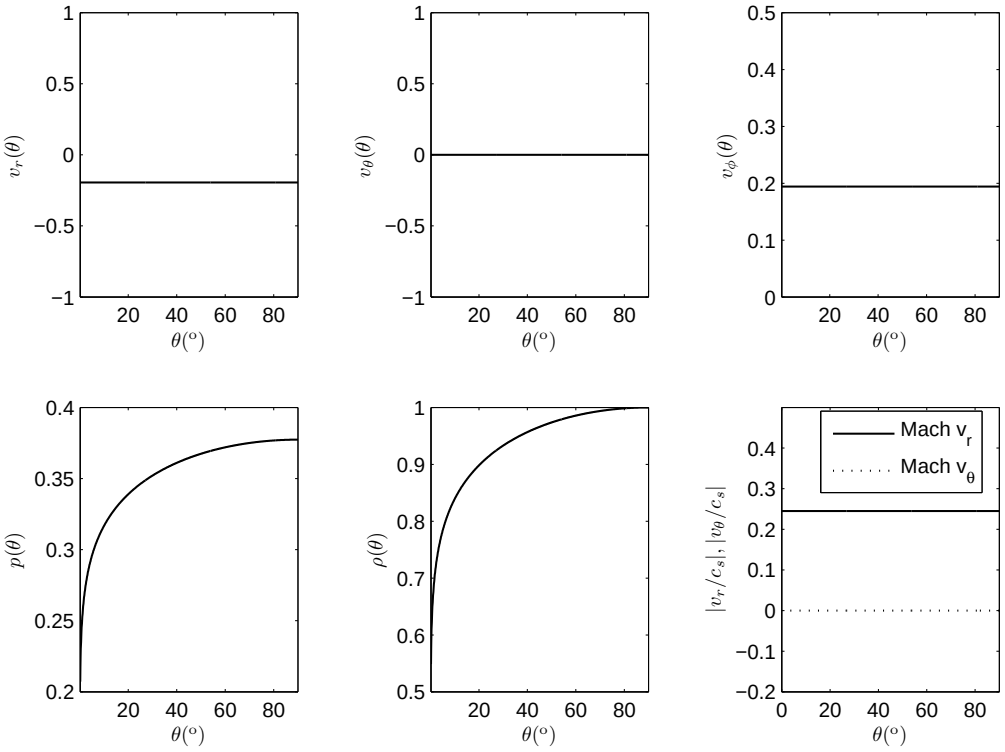

Fig. 7.— The solution corresponding to $\epsilon\prime = 0.1$ in NY95. Here $\alpha = 0.1$, $n = 1.5$, $f = 1$ and $\gamma_{\rm equ} = 1.6061$.

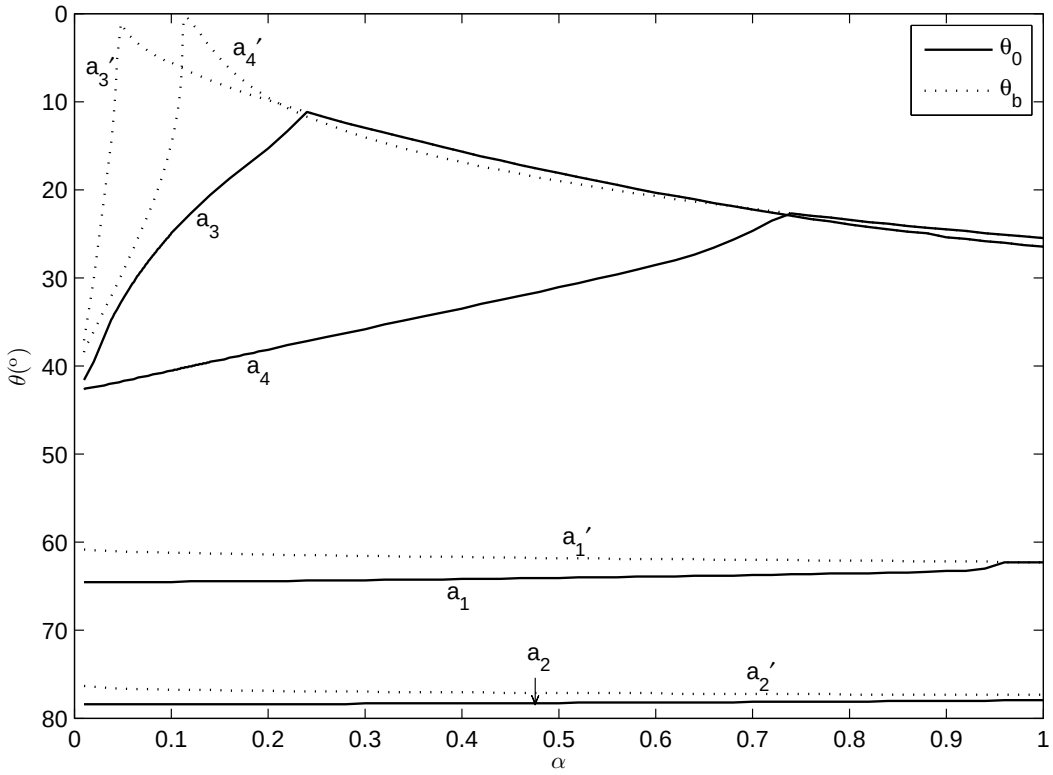

Fig. 8.— Solution dependence on α. Solid lines a_1, a_2, a_3 and a_4 represent the upper boundaries of the inflow region, and dotted lines a_1', a_2', a_3' and a_4' represent the boundaries of the whole inflow/outflow region. All the lines correspond to $n = 1.3$. Lines a_1 and a_1' correspond to $f = 0.01$ and $\gamma_{\rm equ} = 5/3$; lines a_2 and a_2' correspond to $f = 0.01$ and $\gamma_{\rm equ} = 4/3$; lines a_3 and a_3' correspond to $f = 1$ and $\gamma_{\rm equ} = 5/3$; lines a_4 and a_4' correspond to $f = 1$ and $\gamma_{\rm equ} = 4/3$.

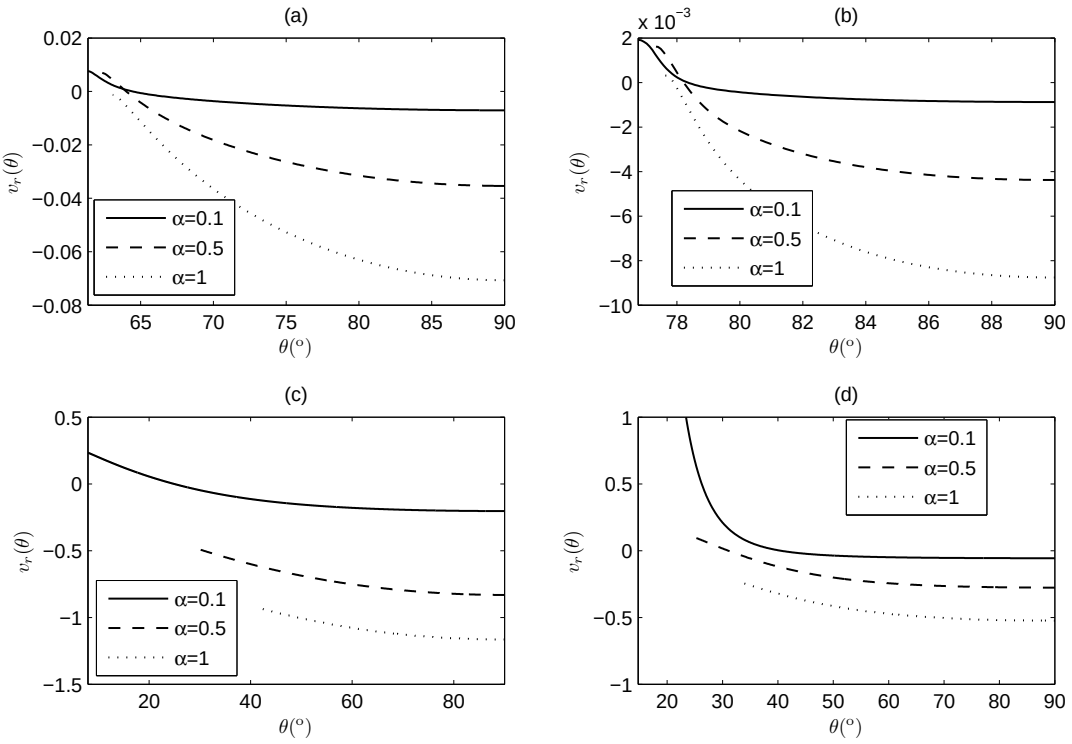

Fig. 9.— The distribution of $v_r(\theta)$ along the θ-direction for solutions with different α. Figure (a) corresponds to $n = 1.3$, $f = 0.01$ and $\gamma_{\rm equ} = 5/3$; Figure (b) corresponds to $n = 1.3$, $f = 0.01$ and $\gamma_{\rm equ} = 4/3$; Figure (c) corresponds to $n = 1.3$, $f = 1$ and $\gamma_{\rm equ} = 5/3$; Figure (d) corresponds to $n = 1.3$, $f = 1$ and $\gamma_{\rm equ} = 4/3$. The solid, dashed and dotted lines correspond to $\alpha = 0.1$, 0.5 and 1, respectively.

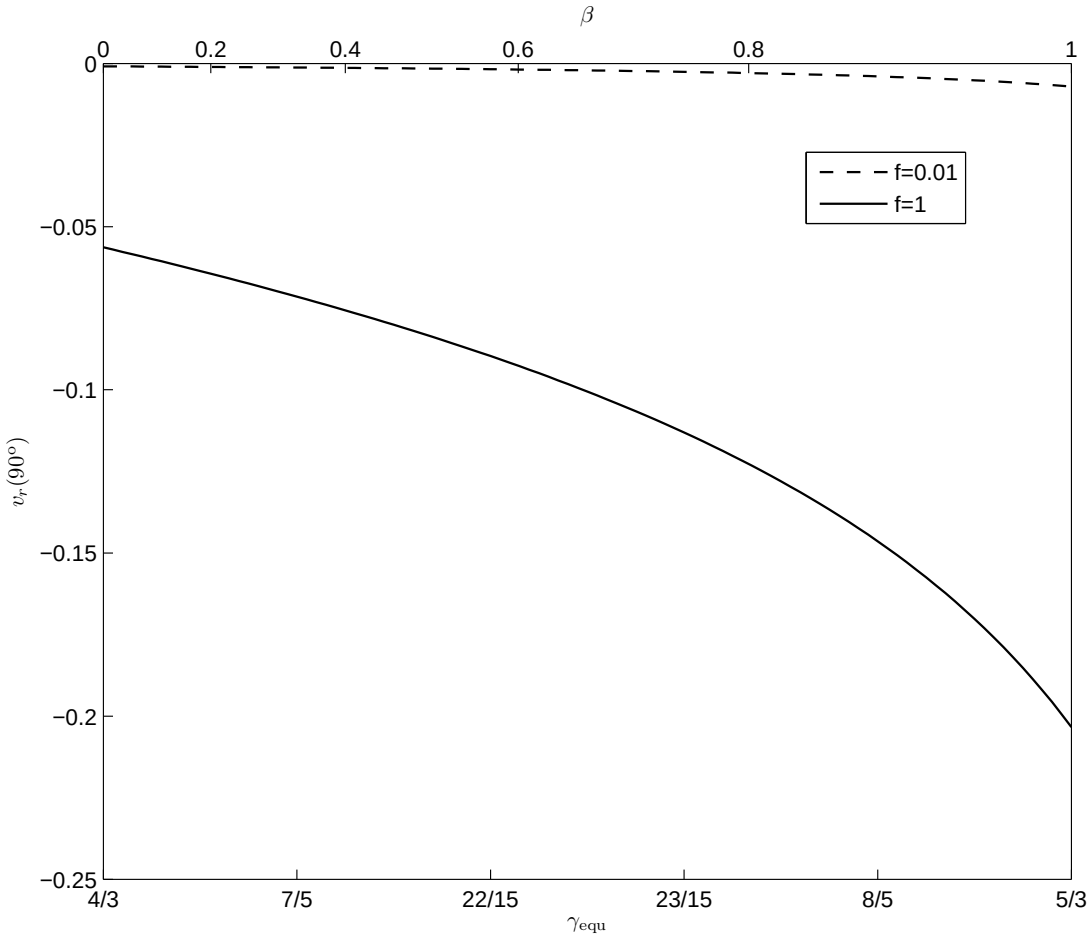

Fig. 10.— The equatorial values of $v_r(\theta)$ corresponding to different $\gamma_{\rm equ}$. All the solutions correspond to $\alpha = 0.1$ and $n = 1.3$. The solid line corresponds to $f = 1$, while the dashed line corresponds to $f = 0.01$. β on the top axis corresponds to $\gamma_{\rm equ}$ on the bottom axis and is calculated based on $\gamma = 5/3$.

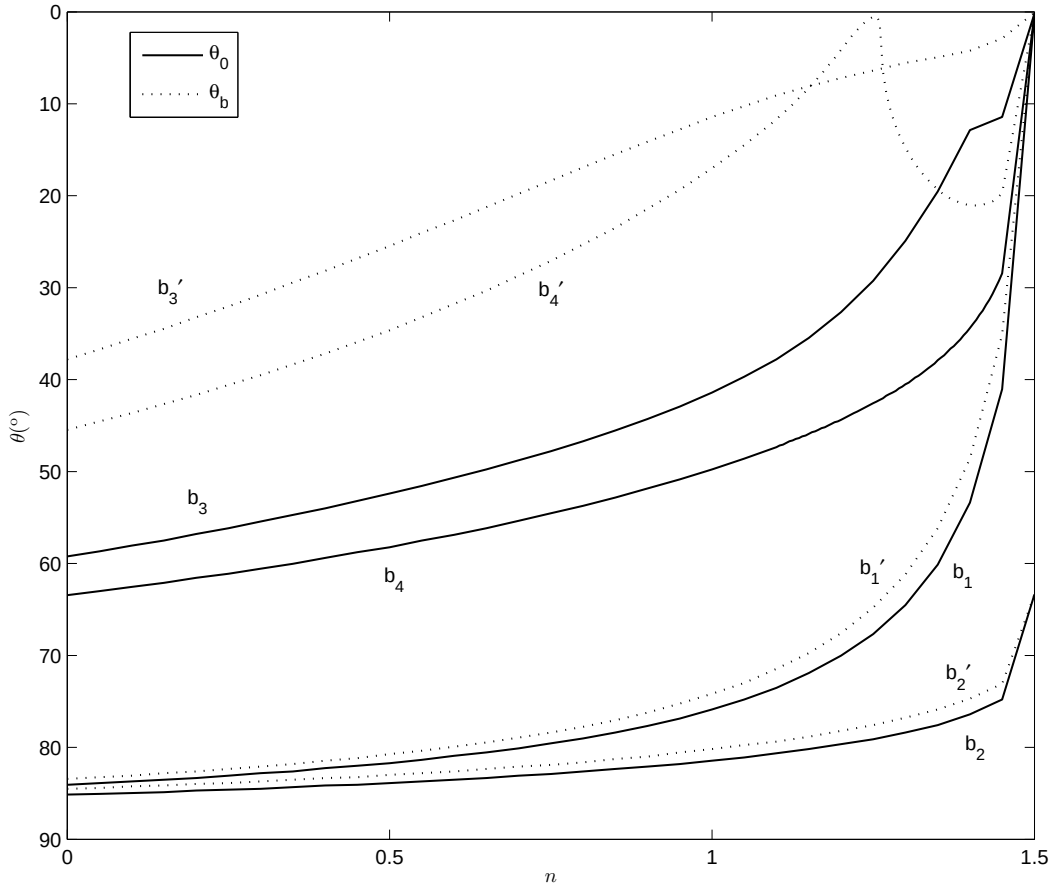

Fig. 11.— Solution dependence on n. Solid lines b_1, b_2, b_3 and b_4 represent the upper boundary of the inflow region, and dotted lines b'_1, b'_2, b'_3 and b'_4 represents the boundaries of the whole inflow/outflow region. All the lines correspond to $\alpha = 0.1$. Lines b_1 and b'_1 correspond to $f = 0.01$ and $\gamma_{\rm equ} = 5/3$; lines b_2 and b'_2 correspond to $f = 0.01$ and $\gamma_{\rm equ} = 4/3$; lines b_3 and b'_3 correspond to $f = 1$ and $\gamma_{\rm equ} = 5/3$; lines b_4 and b'_4 correspond to $f = 1$ and $\gamma_{\rm equ} = 4/3$.

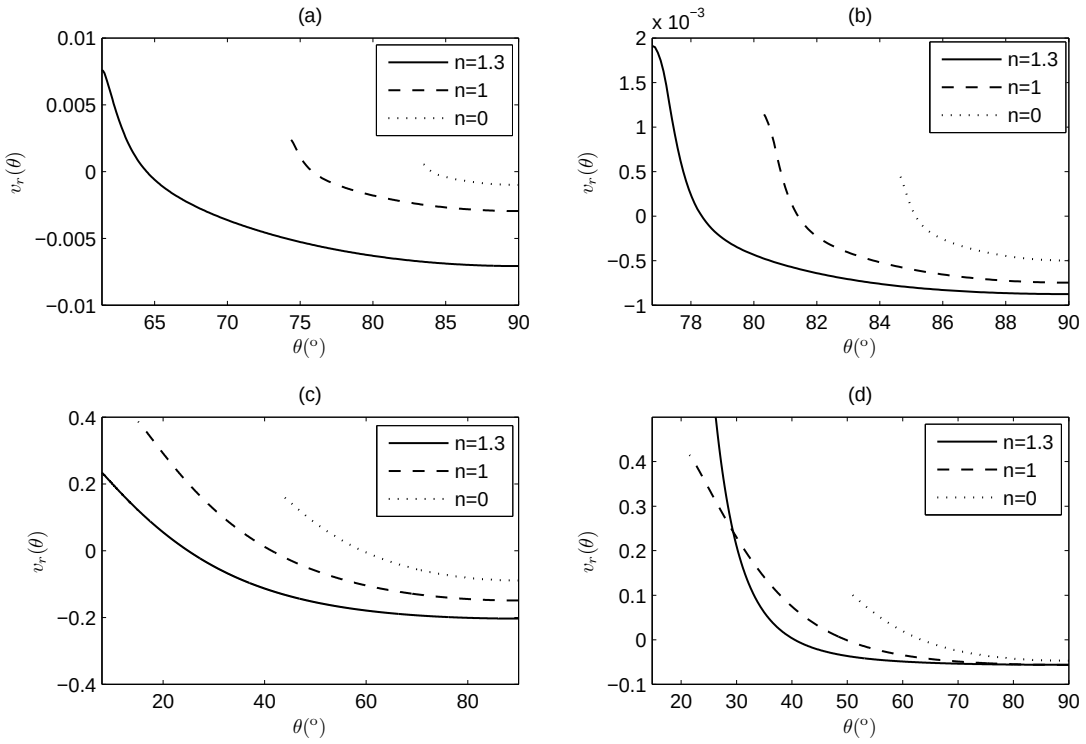

Fig. 12.— The distribution of $v_r(\theta)$ along the θ-direction for solutions with different n. Figure (a) corresponds to $\alpha = 0.1$, $f = 0.01$ and $\gamma_{\rm equ} = 5/3$; Figure (b) corresponds to $\alpha = 0.1$, $f = 0.01$ and $\gamma_{\rm equ} = 4/3$; Figure (c) corresponds to $\alpha = 0.1$, $f = 1$ and $\gamma_{\rm equ} = 5/3$; Figure (d) corresponds to $\alpha = 0.1$, $f = 1$ and $\gamma_{\rm equ} = 4/3$. The solid, dashed and dotted lines correspond to $n = 1.3$, 1 and 0, respectively.

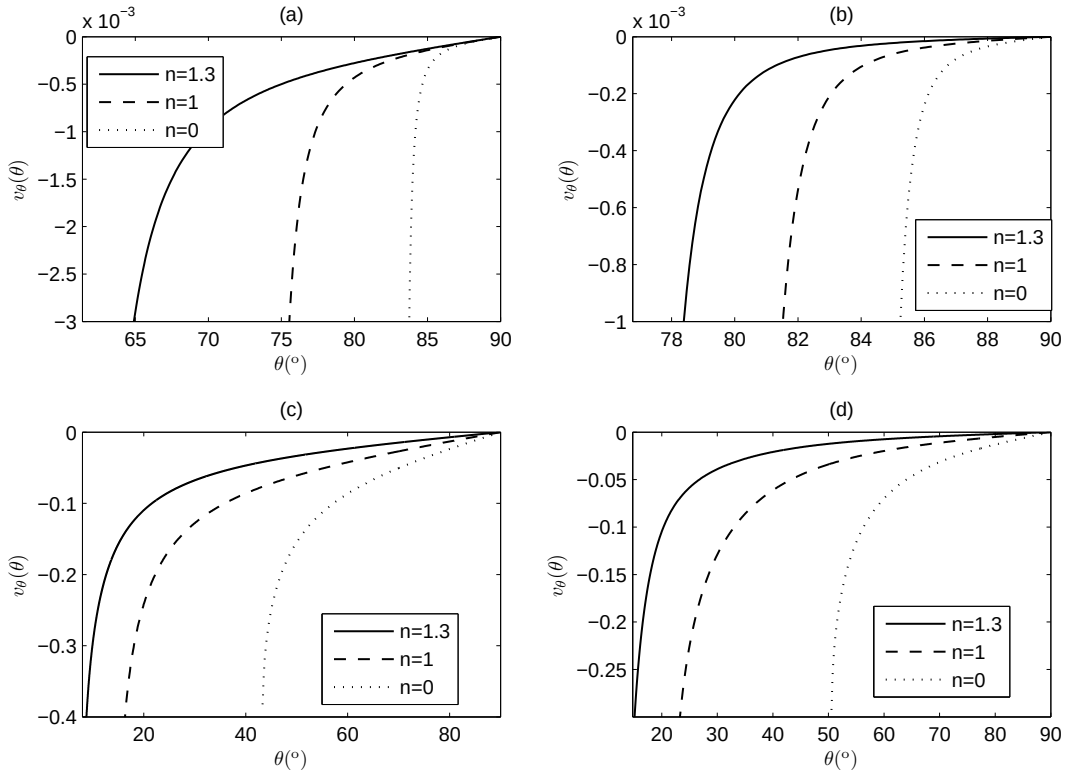

Fig. 13.— The distribution of $v_\theta(\theta)$ along the θ-direction for solutions with different n. Figure (a) corresponds to $\alpha = 0.1$, $f = 0.01$ and $\gamma_{\rm equ} = 5/3$; Figure (b) corresponds to $\alpha = 0.1$, $f = 0.01$ and $\gamma_{\rm equ} = 4/3$; Figure (c) corresponds to $\alpha = 0.1$, $f = 1$ and $\gamma_{\rm equ} = 5/3$; Figure (d) corresponds to $\alpha = 0.1$, $f = 1$ and $\gamma_{\rm equ} = 4/3$. The solid, dashed and dotted lines correspond to $n = 1.3$, 1 and 0, respectively.

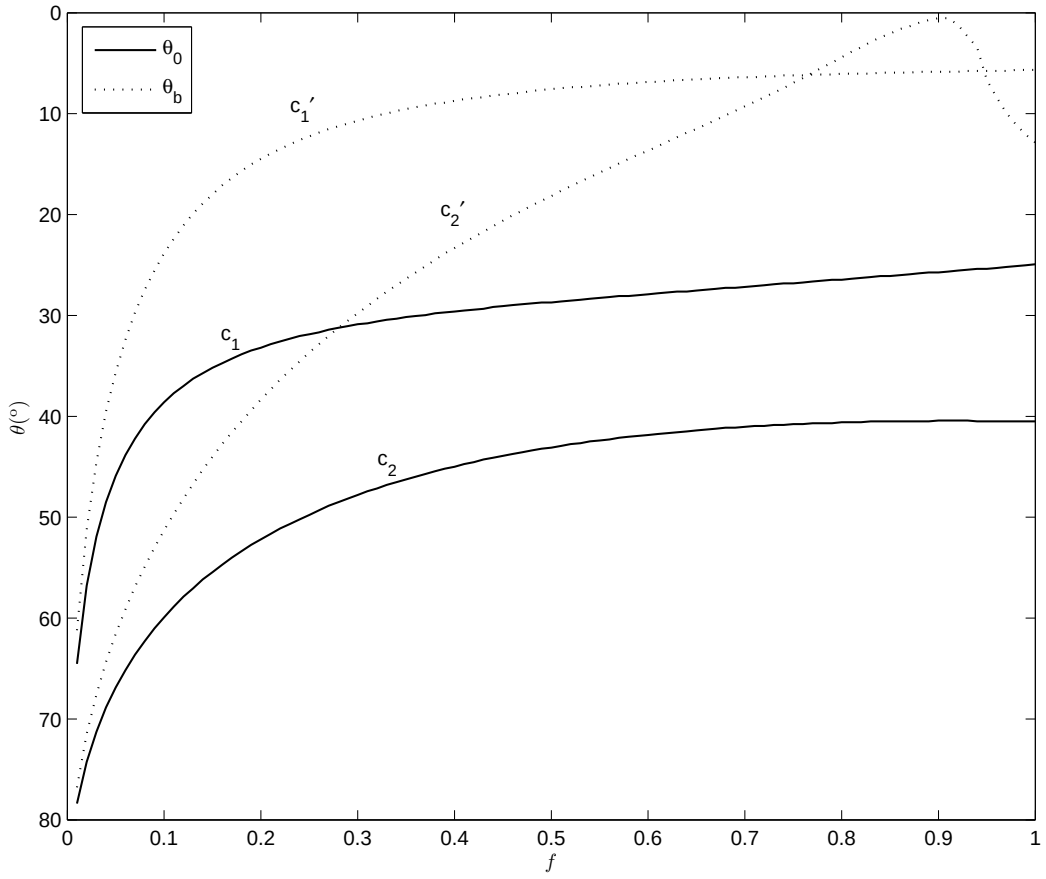

Fig. 14.— Solution dependence on f. Solid lines c_1 & c_2 represent the upper boundary of the inflow region, and dotted lines c_1' & c_2' represents the outer boundary of the whole accretion flow. All the lines correspond to $\alpha = 0.1$ & $n = 1.3$. Lines c_1 and c_1' correspond to $\gamma_{\rm equ} = 5/3$; lines c_2 and c_2' correspond to $\gamma_{\rm equ} = 4/3$.

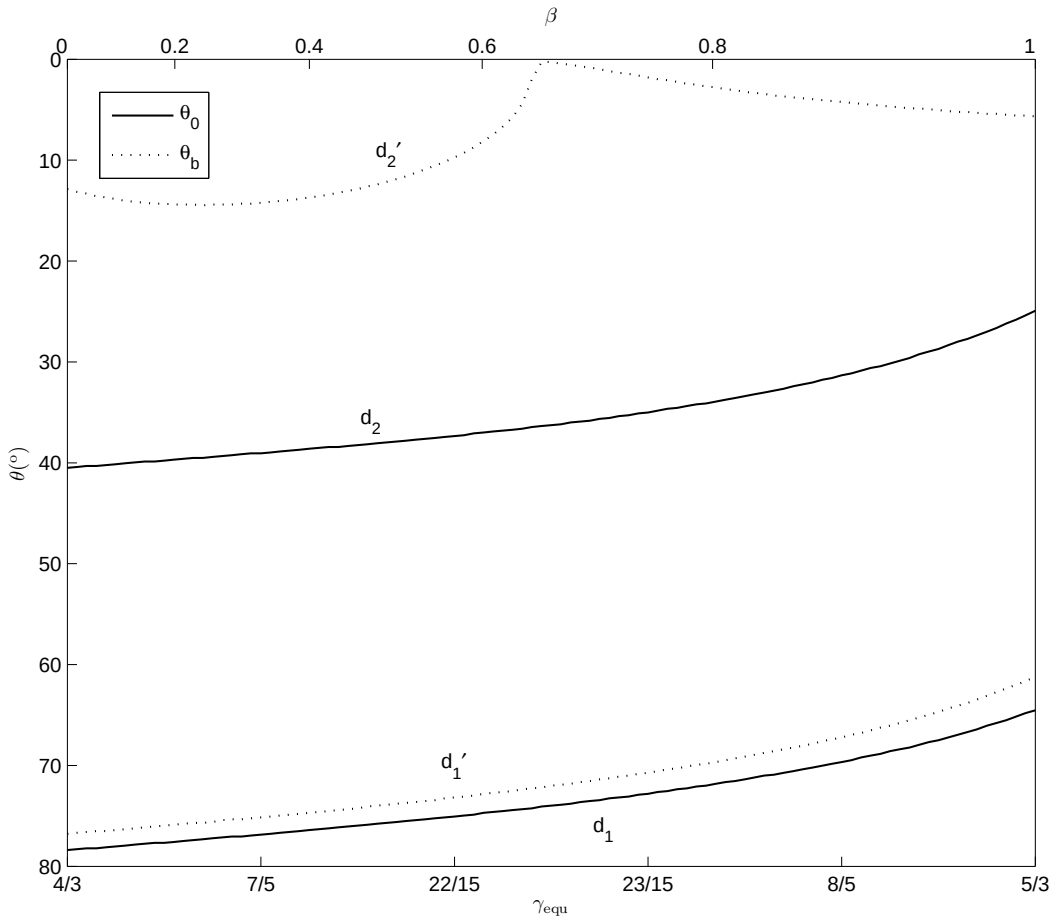

Fig. 15.— Solution dependence on $\gamma_{\rm equ}$. Solid lines d_1 & d_2 represent the upper boundary of the inflow region, and dotted lines d_1' & d_2' represent the upper boundary of the whole inflow/outflow region. All the lines correspond to $\alpha = 0.1$ & $n = 1.3$. Lines d_1 and d_1' correspond to $f = 0.01$; lines d_2 and d_2' correspond to $f = 1$. β on the top axis corresponds to $\gamma_{\rm equ}$ on the bottom axis and is calculated based on $\gamma = 5/3$.

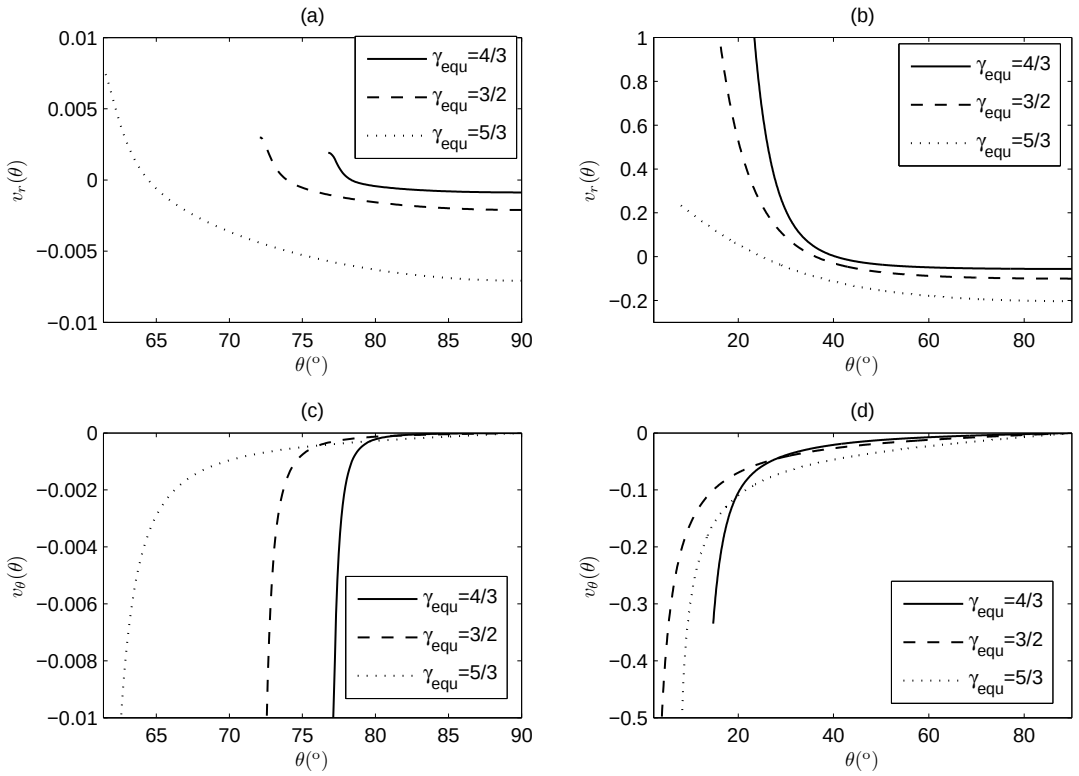

Fig. 16.— The v_r and v_θ distributions along the θ-direction for solutions with different $\gamma_{\rm equ}$. Figures (a) & (c) correspond to solutions with $n = 1.3$, $\alpha = 0.1$ and $f = 0.01$, while Figures (b) & (d) correspond to solutions with $n = 1.3$, $\alpha = 0.1$ and $f = 1$. The solid, dashed and dotted lines correspond to $\gamma_{\rm equ} = 4/3$, 3/2 and 5/3, respectively.

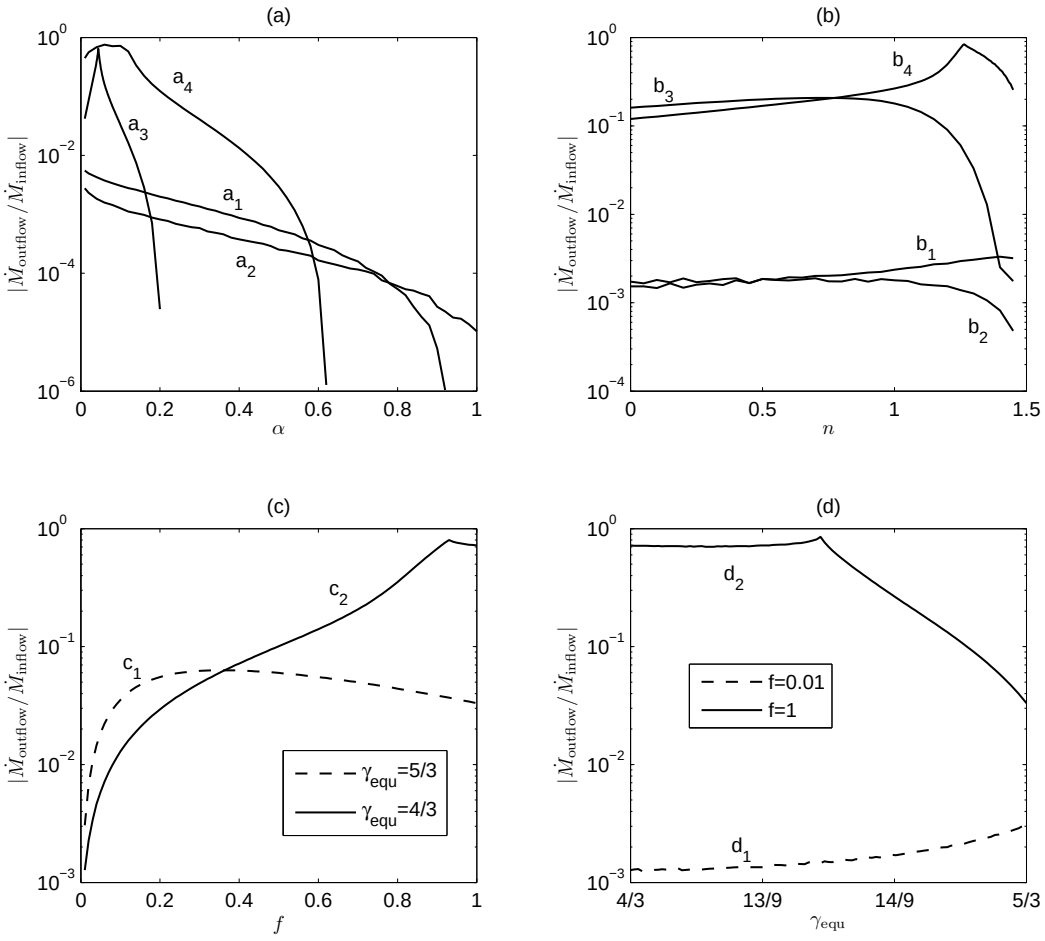

Fig. 17.— The ratio of the outflow rate to the inflow rate. The vertical axes show the absolute values of the ratio, and the horizontal axes correspond to different input parameters. The lines in the top left panel correspond to the lines in Figure 8. The lines in the top right panel correspond to the lines in Figure 11. The lines in the bottom left panel correspond to the lines in Figure 14. The lines in the bottom right panel correspond to the lines in Figure 15. Certain parts of some lines are missing due to that the solutions there don't contain an outflow region.

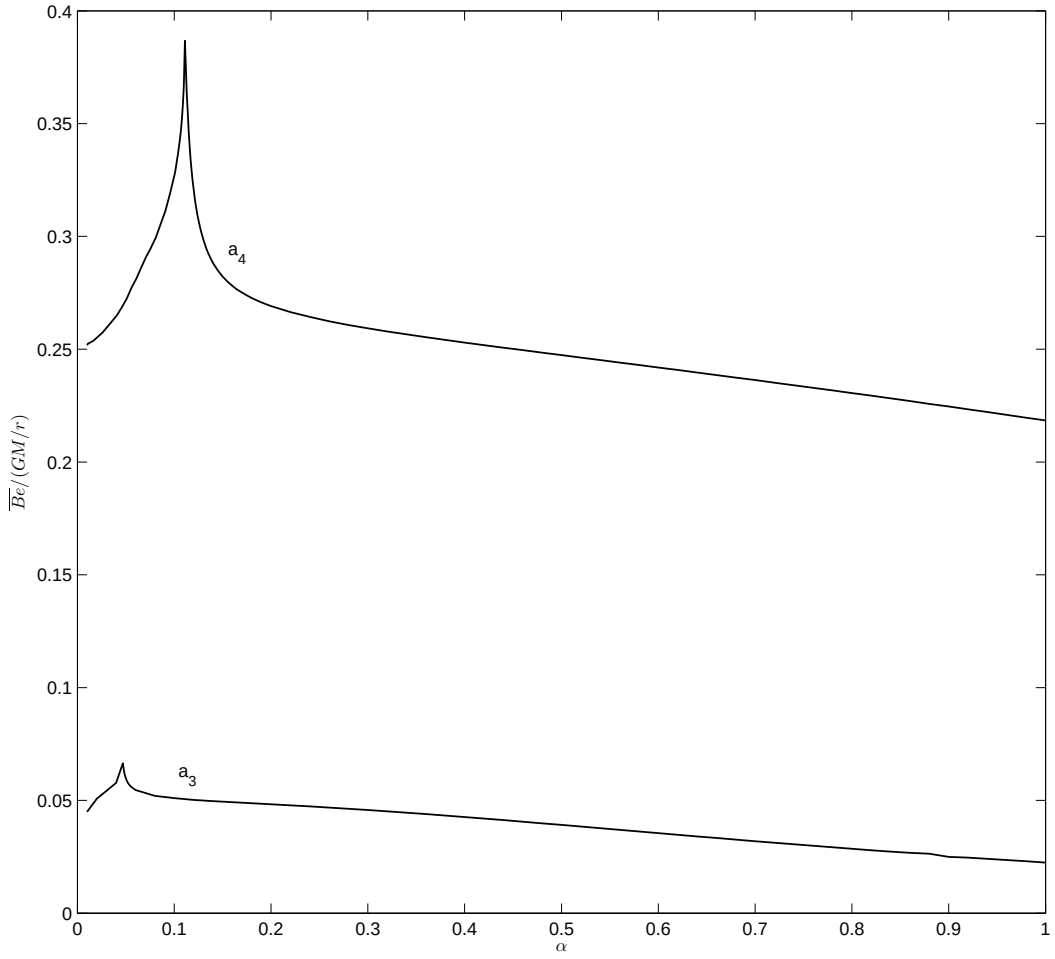

Fig. 18.— The θ-averaged Bernoulli function for variant α. Line a_3 corresponds to solutions with $f = 1$, $\gamma_{\rm equ} = 5/3$ and $n = 1.3$. Line a_4 corresponds to solutions with $f = 1$, $\gamma_{\rm equ} = 4/3$ and $n = 1.3$.

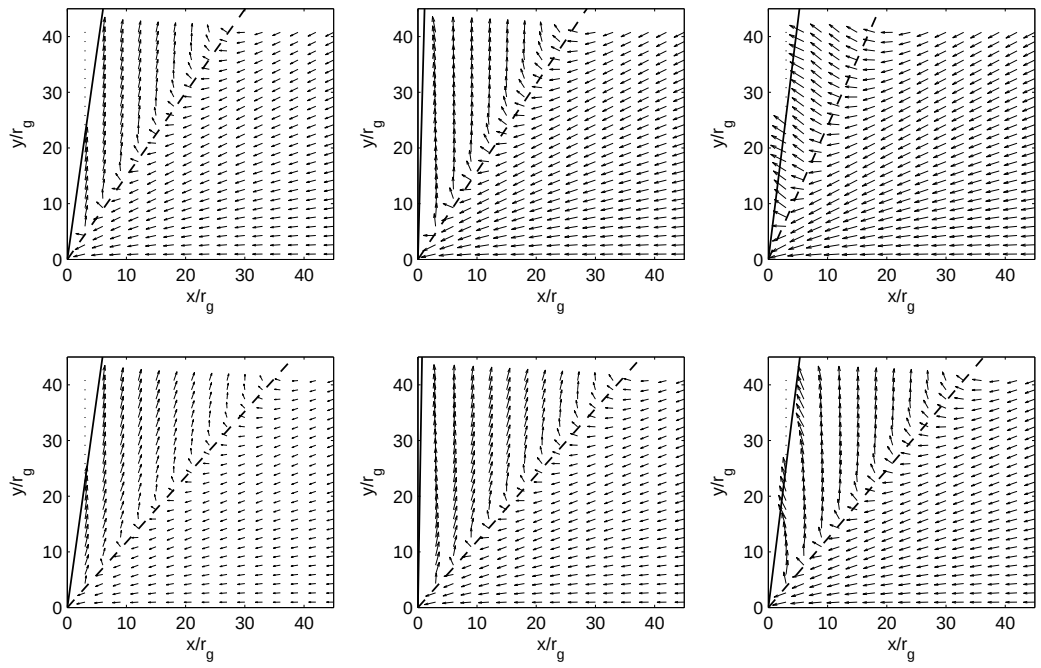

Fig. 19.— The velocity field patterns around the bends for variant α. The first row of figures corresponds to the bend of line a_3' in Figure 8, with $\alpha = 0.043$, 0.05 and 0.12 from left to right respectively, and other parameters $f = 1$, $\gamma_{\rm equ} = 5/3$ and $n = 1.3$. The second row of figures corresponds to the bend of line a_4' in Figure 8, with $\alpha = 0.106$, 0.12 and 0.165 from left to right respectively, and other parameters $f = 1$, $\gamma_{\rm equ} = 4/3$ and $n = 1.3$. The lengths of arrows indicate the absolute values of the vector $\vec{v}_r(\theta)+\vec{v}_\theta(\theta)$, which are scaled logarithmically. The solid lines correspond to the inclination $\theta_{\rm b}$, while the dashed lines correspond to the inclination θ_0.

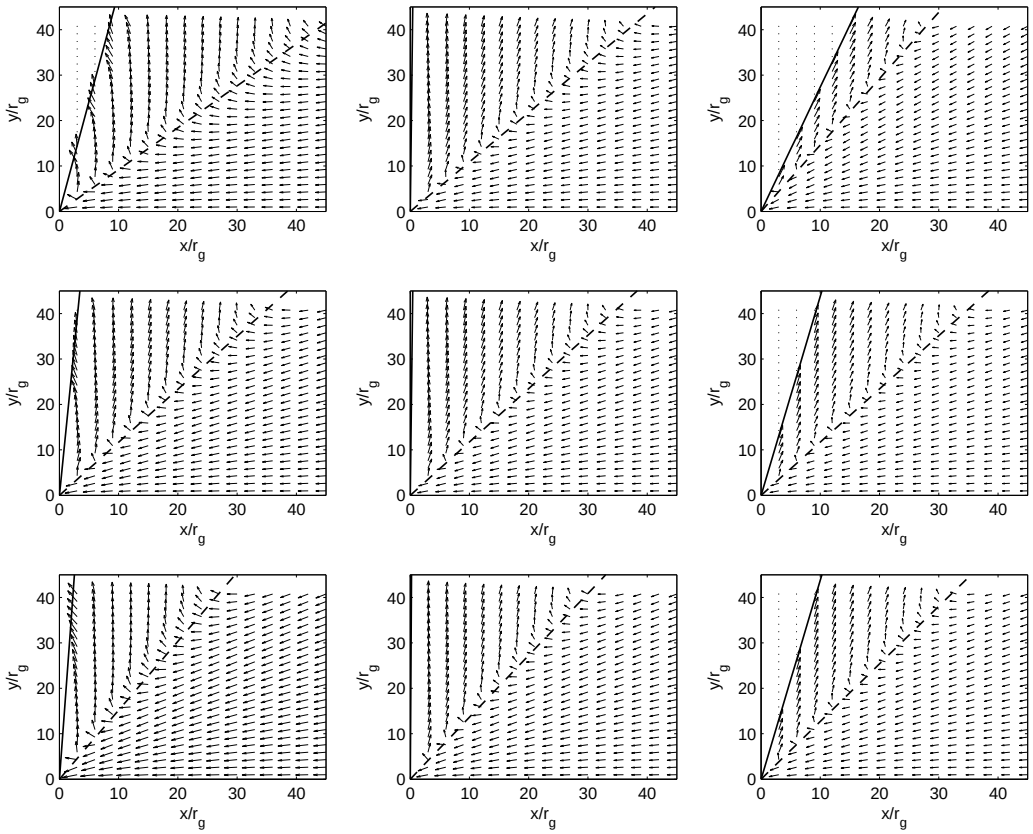

Fig. 20.— The velocity field patterns around the bends for variant n, f and $\gamma_{\rm equ}$. The first row of figures corresponds to the bend of line b_4' in Figure 11, with n = 1.1, 1.25 and 1.4 from left to right respectively, and other parameters α = 0.1, f = 1 and $\gamma_{\rm equ}$ = 4/3. The second row of figures corresponds to the bend of line c_2' in Figure 14, with f = 0.8, 0.9 and 1 from left to right respectively, and other parameters α = 0.1, $\gamma_{\rm equ}$ = 4/3 and n = 1.3. The third row of figures corresponds to the bend of line d_2' in Figure 15, with $\gamma_{\rm equ}$ = 47/30, 3/2 and 43/30 from left to right respectively, and other parameters α = 0.1, f = 1 and n = 1.3. The lengths of arrows indicate the absolute values of the vector $\vec{v_r}(\theta)$+$\vec{v_\theta}(\theta)$, which are scaled logarithmically. The solid lines correspond to the inclination $\theta_{\rm b}$, while the dashed lines correspond to the inclination θ_0.